

## Kronoseismology III: Waves in Saturn's inner C ring

Richard G. French<sup>\*a</sup>, Colleen A. McGhee-French<sup>a</sup>, Philip D. Nicholson<sup>b</sup>, Mathew M. Hedman<sup>c</sup>

<sup>a</sup> Department of Astronomy, Wellesley College, Wellesley, MA 02481, USA

<sup>b</sup> Department of Astronomy, Cornell University, Ithaca, NY 14853, USA

<sup>c</sup> Department of Physics, University of Idaho, Moscow, ID 83844, USA

### ARTICLE INFO

**Keywords:**  
Occultations  
Planets: rings

### ABSTRACT

We investigate waves driven in Saturn's rings by planetary normal modes, concentrating on the previously unexplored inner C ring. In this region, the known waves all have exceptionally short wavelengths, which has proven problematic for previous studies that depended on the accurate estimate of wave phases for wave identification. However, detailed study of over 200 stellar and radio occultations observed by Cassini, involving measurements of  $\sim 65$  circular ring features, has resulted in a radius scale for the rings which has absolute errors of  $\sim 250$  m and internal (relative) uncertainties of  $\sim 150$  m (French et al., 2017). This permits us to measure the phases of waves with wavelengths as short as  $\sim 1$  km, or even less, which has enabled the identification of additional waves in the inner C ring. Using a variety of wavelet-based approaches and employing stellar occultation data acquired by the Visual and Infrared Mapping Spectrometer (VIMS) instrument, we have identified three new Saturn-driven outer Lindblad resonance density waves: W76.02 (radius near 76020 km, wavenumber  $m = -9$ ), W76.44 ( $m = -2$ ), and W76.46 ( $m = -7$ ). We also identify a new class of waves driven by Saturn's internal oscillations: vertical (bending) waves W74.67 ( $m = -7$ ), W74.93 ( $m = -4$ ), W74.94 ( $m = -9$ ), and W76.24 ( $m = -8$ ). All of these identifications are based on the three observational parameters that can be derived from the wave profiles: their  $m$ -values (or number of spiral arms), their pattern speeds  $\Omega_p$ , and their directions of propagation. These results, when combined with previous identifications of Saturn-driven waves, provide significant constraints on Saturn's internal structure.

### 1. Introduction

Spiral density and bending waves are among the most-studied and best-understood dynamical features in Saturn's rings, and have provided a rich trove of information on the surface mass density and viscosity of the principal ring regions (Shu, 1984; Esposito et al., 1984; Colwell et al., 2009). The majority of these waves are driven at resonances with external satellites, particularly in the A and B rings. In recent years, however, a second set of waves has been identified, primarily in the C ring, that are driven not by satellites but by irregularities in Saturn's own gravity field. The first such waves were described by Rosen et al. (1991), based on a single ring radio occultation observed by the Voyager spacecraft in 1980, and ascribed to low-order normal mode oscillations in Saturn by Marley and Porco (1993). But it was not until the advent of the Cassini mission, with the accompanying flood of occultation data, that it was possible to verify this hypothesis and identify individual waves with specific internal oscillations. Hedman and Nicholson (2013), using a wavelet-based approach and employing stellar occultation data acquired by the Visual and Infrared

Mapping Spectrometer (VIMS) instrument, were able to identify six density waves in the middle C ring (including four of the original Rosen waves) with fundamental sectoral modes ( $f$ -modes with  $m = \ell$ ) in Saturn. They were able to do this by combining data from multiple occultations to determine both the number of spiral arms in each wave  $m$ , and its rotation rate, or *pattern speed*,  $\Omega_p$ . The measured frequencies of such modes provide important, and heretofore unavailable, information on Saturn's internal structure and rotation rate. These initial wave identifications ranged from  $m = 2$  to  $m = 4$ , with two different waves being identified with  $m = 2$  and three with  $m = 3$ .

In a follow-up study using the same techniques and an expanded occultation data set, Hedman and Nicholson (2014) identified seven additional density waves in the middle C ring, including two more driven by normal modes with  $m = 1$  and  $m = 10$ . An unexpected result of this study was the identification of a second class of Saturnian waves, with  $m = 3$  and pattern speeds of  $808\text{--}834^\circ \text{ d}^{-1}$ , similar to the planet's own rotation rate. Unlike the sectoral modes, which represent normal modes of oscillation within the planet analogous to those seen in the Earth and Sun, these new waves are evidently driven by gravitational

\* Corresponding author.

E-mail address: [rfranch@wellesley.edu](mailto:rfranch@wellesley.edu) (R.G. French).

irregularities fixed in the planet, or tesseral harmonics of Saturn's gravity field. The tesseral resonances in the C ring occur where the local orbital angular velocity  $n \approx (3/2)\omega_p$ , where  $\omega_p$  is the planet's rotation rate. The pattern speeds of the tesseral waves are much lower than those driven by f-modes within Saturn.

In yet another study, French et al. (2016) investigated the prominent wavelike structure within the eccentric Maxwell ringlet and used wavelet analysis to identify the strongly non-linear wave as a 2-armed trailing spiral, consistent with a density wave driven by a third  $m = 2$  normal mode within Saturn. In this case, the radial wavelength of the wave is rhythmically compressed and stretched by the eccentricity profile across the ringlet, resulting in a complex pattern of radial variations with longitude.

In this paper, we present further studies of waves driven in Saturn's rings by planetary normal modes, concentrating on the previously unexplored inner C ring. In this region, the known waves all have exceptionally short wavelengths, which has proven problematic for previous investigations that depended on the accurate estimate of wave phases. However, detailed study of over 200 stellar and radio occultations observed by Cassini, involving measurements of  $\sim 65$  circular ring features, has resulted in a radius scale for the rings with absolute errors of  $\sim 250$  m and internal (relative) uncertainties of  $\sim 150$  m (French et al., 2017). This permits us to measure the phases of waves with wavelengths as short as  $\sim 1$  km, or even less, which has enabled us to identify three additional Saturn-driven density waves in the inner C ring. We also identify four vertical (or bending) waves, representing a new category of waves driven by Saturn's internal oscillations. After some brief theoretical background on normal modes and wave geometry in Section 2, we describe the features chosen for detailed study in Section 3. In Section 4 we outline our methods of analysis, and our principal results are presented in Sections 5–7. We summarize our conclusions and suggest some avenues for future work in Section 8.

## 2. Theoretical background

Both normal modes and tesseral harmonics are classified by their surface geometry, which for a non-rotating planet can be described in terms of the usual spherical harmonics,  $Y_\ell^m(\theta, \psi) = P_\ell^m(\cos \theta) \cos(m\psi)$ , where  $\theta$  is the colatitude,  $\psi$  is the longitude in a planet-fixed reference frame and  $P_\ell^m(x)$  is an associated Legendre polynomial. The parameter  $\ell$  specifies the total number of nodal circles on the surface of the planet, while  $-\ell \leq m \leq \ell$ .  $|m|$  is the number of these nodal circles that pass through both poles, the other  $\ell - |m|$  being parallel to lines of latitude. Sectoral modes, which include all Saturn normal modes identified to date, have  $|m| = \ell$ , implying that they have no nodal lines parallel to the equator. Such modes, which have longitudinal structure but no variations in sign with latitude, have long been expected to be the most effective in exerting a periodic gravitational influence on the rings (Marley and Porco, 1993).

In the reference frame of the planet, the angular and temporal variations in the gravity field associated with such a normal mode can be expressed in the form (Marley and Porco, 1993)

$$U(\theta, \psi, t) = P_\ell^m(\cos \theta) e^{i[m\psi - \sigma_{\ell m}^0 t]}, \quad (1)$$

where  $\sigma_{\ell m}^0$  is the frequency of the mode's oscillation. (The superscript 0 refers to the frequency in the non-rotating frame.) For a non-rotating planet,  $\sigma_{\ell m}^0$  is independent of  $m$ , but for a rotating planet it is given to first order in the spin rate  $\omega_p$  by the expression

$$\sigma_{\ell m}^0 \approx \sigma_\ell^0 - mC_\ell \omega_p, \quad (2)$$

**Table 1**  
VIMS stellar occultations used.

Star/rev <sup>a</sup>	Date (year)	$B_\star$ <sup>b</sup> (deg)	$B_{\text{eff}}$ <sup>c</sup> (deg)	$\beta$ <sup>d</sup>
RHyA036I	2007.001	− 29.4	76.3	0.24
alpAur041I	2007.223	50.9	53.3	0.75
RCas065I	2008.303	56.0	− 56.0	− 0.67
gamCru071I	2008.435	− 62.3	70.8	0.35
gamCru073I	2008.474	− 62.3	71.1	0.34
gamCru078I	2008.571	− 62.3	71.6	0.33
gamCru079I	2008.589	− 62.3	72.3	0.32
gamCru081I	2008.629	− 62.3	72.6	0.31
gamCru082I	2008.649	− 62.3	72.8	0.31
gamCru086I	2008.730	− 62.3	73.2	0.30
gamCru089I	2008.791	− 62.3	73.3	0.30
gamCru093I	2008.874	− 62.3	64.0	0.49
gamCru094I	2008.894	− 62.3	67.9	0.41
gamCru096I	2008.937	− 62.3	70.0	0.36
gamCru100I	2009.032	− 62.3	62.4	0.52
gamCru101I	2009.058	− 62.3	62.4	0.52
gamCru102I	2009.085	− 62.3	62.4	0.52
betPeg104I	2009.155	31.7	− 45.0	− 1.00
betPeg172I	2012.727	31.7	− 71.6	− 0.33
WHya179I	2013.052	− 34.6	− 68.5	− 0.39
WHya180I	2013.089	− 34.6	− 69.3	− 0.38
WHya181I	2013.125	− 34.6	− 69.6	− 0.37
muCep185E	2013.246	59.9	− 63.5	− 0.50
RCas185I	2013.248	56.0	− 75.7	− 0.26
gamCru187I	2013.306	− 62.3	81.7	0.15
gamCru187E	2013.307	− 62.3	62.9	0.51
muCep191I	2013.406	59.9	− 80.7	− 0.16
RCas191I	2013.408	56.0	80.1	0.17
muCep193I	2013.471	59.9	− 80.6	− 0.17
RCas194E	2013.507	56.0	− 62.7	− 0.52
2Cen194I	2013.517	− 40.7	− 82.2	− 0.14
RLyr198I	2013.790	40.8	− 66.6	− 0.43
RLyr199aI	2013.921	40.8	74.1	0.28
RLyr200I	2014.008	40.8	− 71.9	− 0.33
L2Pup201bI	2014.137	− 41.9	58.9	0.60
alpLyr202aI	2014.181	35.2	− 55.4	− 0.69
RLyr202bE	2014.182	40.8	− 81.1	− 0.16
L2Pup205bE	2014.478	− 41.9	60.6	0.56
alpLyr206I	2014.539	35.2	− 84.8	− 0.09
L2Pup206E	2014.563	− 41.9	− 52.4	− 0.77
RLyr208E	2014.716	40.8	− 67.8	− 0.41
alpLyr209E	2014.804	35.2	− 84.7	− 0.09
XOph213I	2015.198	5.5	40.1	1.19
alpSco241bE	2016.663	− 32.2	− 78.8	− 0.20
alpSco243E	2016.728	− 32.2	− 82.0	− 0.14
RCas243I	2016.732	56.0	− 62.4	− 0.52
alpSco245I	2016.782	− 32.2	− 41.7	− 1.12
alpSco245E	2016.782	− 32.2	− 85.0	− 0.09
gamCru255I	2017.003	− 62.4	86.9	0.05
gamCru264I	2017.180	− 62.4	87.9	0.04
lamVel268I	2017.257	− 43.8	54.3	0.72
gamCru268I	2017.258	− 62.4	88.4	0.03
alpOri268E	2017.263	11.7	− 29.2	− 1.79
VYCMa269I	2017.273	− 23.4	36.9	1.33
gamCru269I	2017.278	− 62.4	88.5	0.03
alpOri269E	2017.283	11.7	− 24.7	− 2.17
alpCMa274E	2017.364	− 13.5	− 26.3	− 2.02
gamCru276I	2017.404	− 62.4	88.1	0.03
alpOri277I	2017.425	11.7	19.1	2.88
gamCru282I	2017.511	− 62.4	− 88.9	− 0.02
gamCru291I	2017.670	− 62.4	− 84.9	− 0.09
gamCru292I	2017.688	− 62.4	− 84.6	− 0.10

<sup>a</sup> Star name, Cassini orbit number, I (ingress) or E (egress)

<sup>b</sup> Elevation angle of star.

<sup>c</sup> Effective elevation angle in inner C ring near 76,000 km radius (see text).

<sup>d</sup>  $\beta = (\tan B_{\text{eff}})^{-1}$

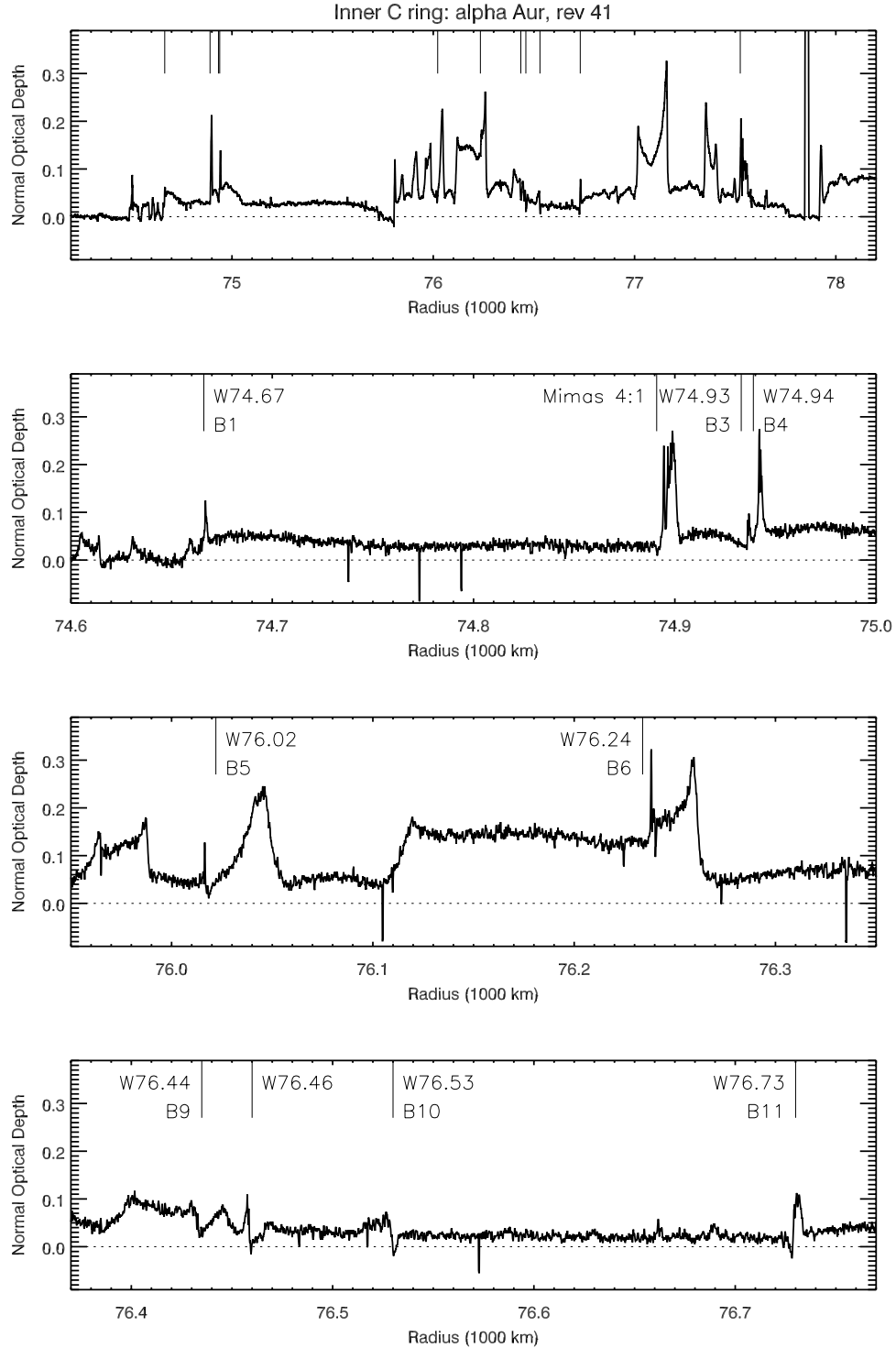


**Fig. 1.** An optical depth profile of the inner C ring, illustrating the context for the wave features examined in this work (see Table 2). The upper panel shows the inner 4000 km of the C ring, while the remaining three panels show the regions around the waves of interest at 1 km resolution and at 10 times larger scale. Also identified are the Mimas 4:1 density wave and, in the upper panel, the Titan - 1:0 bending wave at 77525 km. Note that wave W76.24 (Baillié et al. (2011) feature B6) is located within a plateau feature, designated P1 by Colwell et al. (2009). Data from the VIMS occultation of  $\alpha$  Aurigae on rev 41.

where  $C_\ell$  is a mode-splitting coefficient that is of order unity for small  $\ell$ . In reality, Saturn's spin rate is fast enough to require a model that is second- or even third-order in  $\omega_p$  to obtain reasonably accurate mode frequencies. This can also lead to mixing of  $f$ - and  $g$ -modes, if the latter exist in the deep interior (Fuller et al., 2014).

The planet's rotation, of course, carries the modes along, resulting in a potential seen in the inertial frame that is given by

$$U(\theta, \lambda, t) = P_\ell^m(\cos \theta) e^{i[m(\lambda - \Omega_p t)]}, \quad (3)$$

where  $\lambda$  is the inertial longitude and the pattern speed  $\Omega_p$  is given by

$$\Omega_p = \sigma_{\ell m}^0/m + \omega_p \simeq \sigma_\ell^0/m + (1 - C_\ell) \omega_p. \quad (4)$$

Marley and Porco (1993) and Marley (2014) tabulate theoretical values of  $\sigma_{\ell m}^0$  and the pattern rotation period  $2\pi/\Omega_p$  for saturnian  $f$ -modes with

**Table 2**  
Waves in the inner C ring.

Radius <sup>a</sup> (km)	Rosen <sup>b</sup>	Baillié <sup>c</sup>	Colwell <sup>d</sup>	Propagation direction	References
74666		B1	W74.67	out	this work
74892	a	B2		out	Mimas 4:1 ILR; Rosen et al. (1991)
74933		B3	W74.93	out	this work
74939	b	B4	W74.94	out	this work
76022		B5	W76.02	in	this work
76234		B6	W76.24	out	this work; within P1
76435		B9	W76.44	in	this work
76460				in	this work, designated W76.46
76529		B10		?	designated W76.53
76729		B11	W76.73	?	
77520	c	B12		out	Titan -1:0 IVR; Rosen and Lissauer (1988)

<sup>a</sup> Approximate resonance radius,  $a_{\text{res}}$  (see Table 3 for results of fits to waves studied in this work).

<sup>b</sup> Rosen et al. (1991)

<sup>c</sup> Baillié et al. (2011)

<sup>d</sup> Colwell et al. (2009)

$2 \leq \ell \leq 8$ . Both prograde ( $m > 0$ ) and retrograde ( $m < 0$ ) modes are possible, but only the former are likely to lead to resonances in the rings, as most modes with  $m < 0$  are also retrograde in inertial space (Marley and Porco, 1993). We shall henceforth consider only  $f$ -modes with  $m > 0$ . Predicted  $f$ -mode pattern speeds for Saturn range from  $\Omega_p \simeq 1870^\circ \text{ d}^{-1}$  to  $\sim 1130^\circ \text{ d}^{-1}$  for  $2 \leq \ell \leq 35$  (C. Mankovich 2017, priv. comm.), decreasing slowly with increasing  $\ell$  but increasing rapidly with  $\ell - m$ .

If the quantity  $\ell - m$  is even (or zero), then the resulting potential component is non-zero in the equatorial (or ring) plane and its radial gradient will lead to a periodic radial force on particles orbiting in the rings. At the location in the rings where this frequency, as experienced by a ring particle, equals the local epicyclic frequency  $\kappa$  these periodic forces lead to resonant excitation of the particle's orbital eccentricities, and eventually the generation of a density wave (see Shu (1984) for a full discussion of the theory of wave generation in planetary rings). In terms of  $\kappa$  and the orbital mean motion  $n$ , the resonance condition can be written

$$m(n - \Omega_p) = \kappa, \quad (5)$$

or in terms of the apsidal precession rate  $\dot{\omega} = n - \kappa$ ,

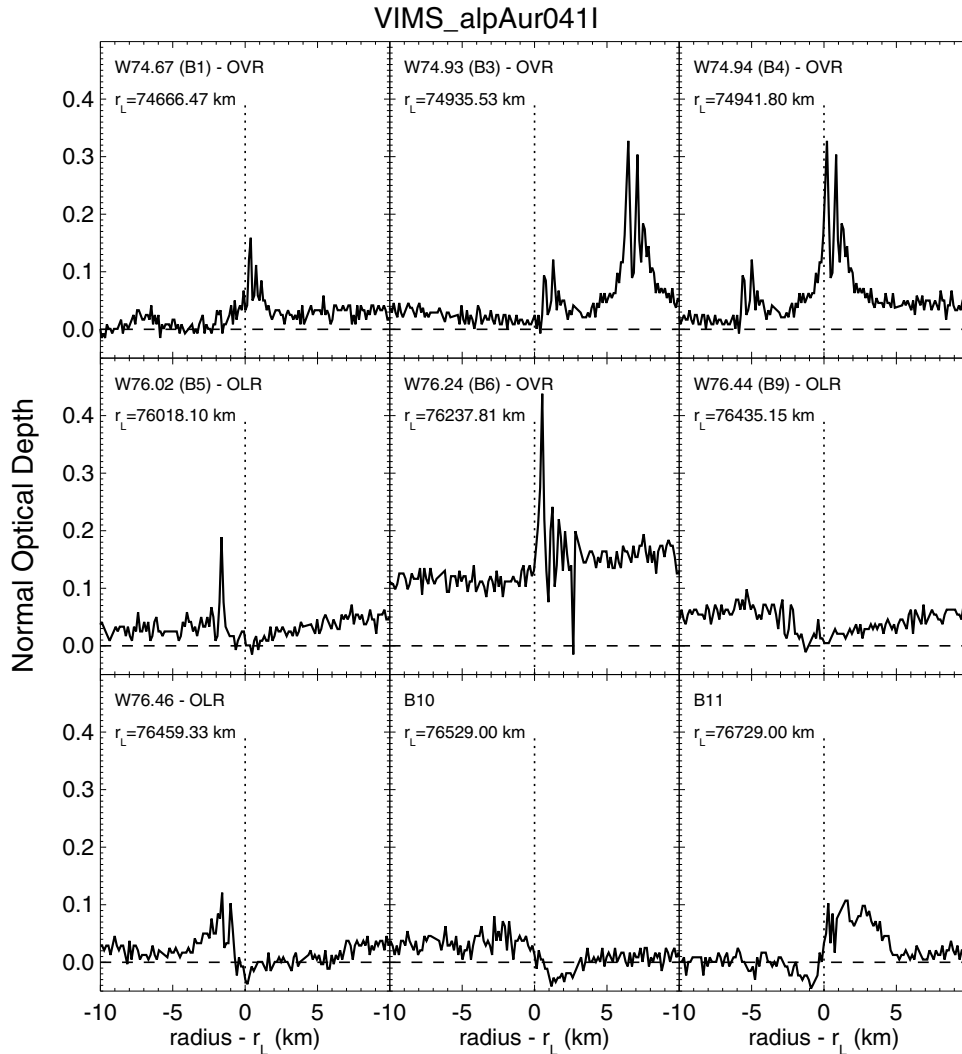


**Fig. 2.** Optical depth profiles of the nine inner C ring waves, in order of increasing orbital radius, as observed in the ingress occultation of  $\alpha$  Aurigae on rev 41, on 23 March 2007. The waves that have been identified in this study are designated by their standard codes plus either the designation OLR (outer Lindblad resonance) for inward-propagating density waves or OVR (outer vertical resonance) for outward-propagating bending waves. Features W76.53 (B10) and W76.73 (B11) have uncertain propagation directions and have not yet been identified. A vertical dotted line indicates the inferred location of the resonance responsible for each wave, as derived in the present work and listed in Table 3. (Approximate values are given in Table 2 for the latter two waves.) Note that waves W74.93 (B3) and W74.94 (B4) are separated by only 6 km, and thus appear in both the second and third panels. The optical depth background is highest for wave W76.24 (B6), which is located within plateau P1.

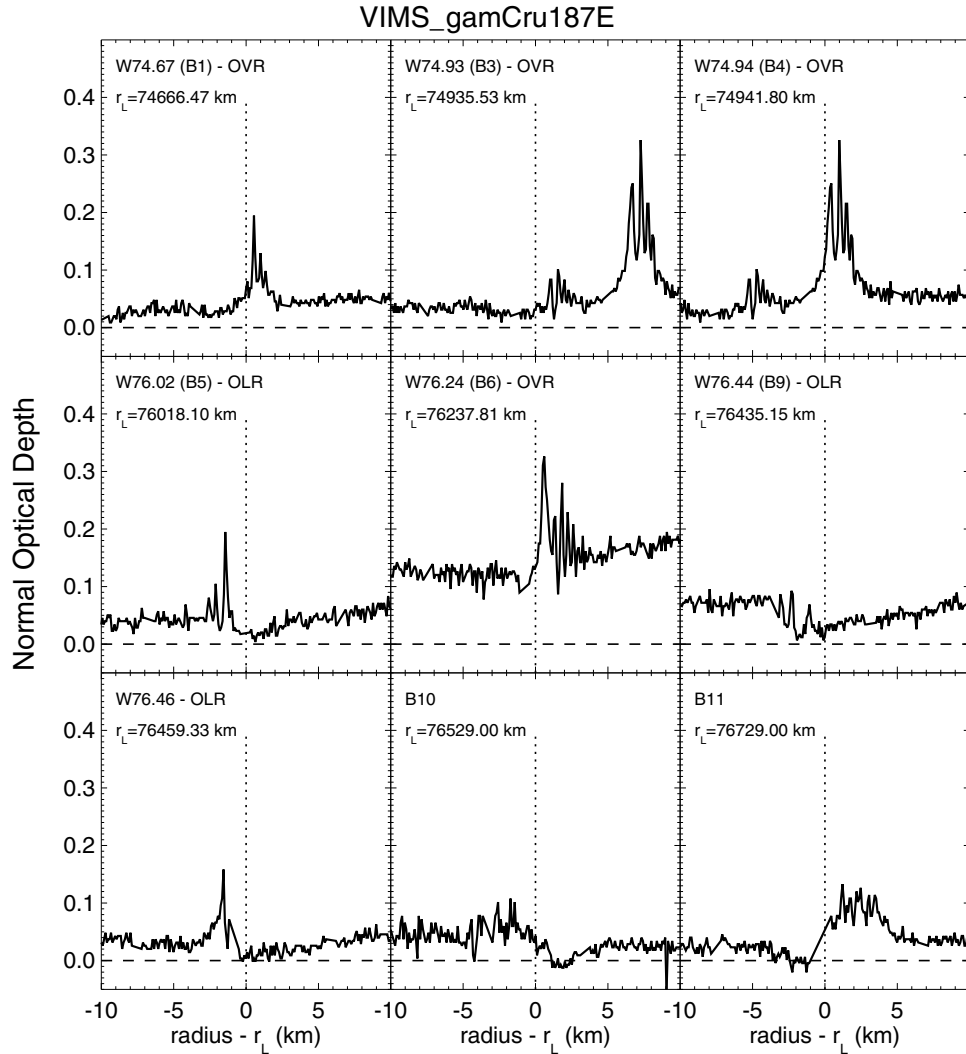


**Fig. 3.** Optical depth profiles of the nine inner C ring waves as observed in the egress occultation of  $\gamma$  Crucis on rev 187, on 22 April 2013, following the same format as Fig. 2.

$$(m - 1)n + \dot{\varpi} = m\Omega_p. \quad (6)$$

Such a location is referred to as a Lindblad resonance. Resonances with  $m > 0$  are known as inner Lindblad resonances (ILRs), and have  $n > \Omega_p$ . Most resonances with external satellites fall into this category, since  $\Omega_p = n_{\text{sat}}$  for the strongest such resonances. Resonances with  $m < 0$  are known as outer Lindblad resonances (OLRs), and have  $n < \Omega_p$ . Since mean motions in the C ring range from  $1100^\circ \text{ d}^{-1}$  to  $1500^\circ \text{ d}^{-1}$ , most Lindblad resonances associated with low- $\ell$  planetary  $f$ -modes are OLRs.<sup>1</sup> Density waves propagate outwards from ILRs and inwards from OLRs (Shu, 1984).

These are not, however, the only type of resonance that can be driven by planetary normal modes. If the quantity  $\ell - m$  is odd, then the resulting potential component is antisymmetric north-south and the associated radial forces are zero in the equatorial plane. In this case,

however, there will be a force normal to the ring plane due to the north-south potential gradient that will lead to a periodic *vertical* force on particles orbiting in the rings. At the location in the rings where this frequency as experienced by a ring particle, equals the local vertical frequency  $\nu$ , these periodic forces lead to resonant excitation of the particle's orbital inclinations, and eventually the generation of a bending wave (Shu, 1984; Shu et al., 1983). In terms of  $\nu$  and the orbital mean motion  $n$ , the resonance condition can be written

$$m(n - \Omega_p) = \nu, \quad (7)$$

or in terms of the nodal regression rate  $\dot{\Omega} = n - \nu$ ,

$$(m - 1)n + \dot{\Omega} = m\Omega_p. \quad (8)$$

Such a location is referred to as a vertical resonance. As above, resonances with  $m > 0$  are known as inner vertical resonances (IVRs), and have  $n > \Omega_p$ , while resonances with  $m < 0$  are known as outer vertical resonances (OVRs), and have  $n < \Omega_p$ . Again, vertical resonances driven by planetary  $f$ -modes are mostly OVRs. The direction of propagation of bending waves is opposite to that of density waves: bending waves propagate inwards from IVRs and outwards from OVRs (Shu, 1984).

For either density or bending waves, the waveform far from the resonance can be written in the asymptotic form

$$f(r, \lambda, t) = A(r)\cos\phi(r, \lambda, t), \quad (9)$$

<sup>1</sup> Note that referring to OLRs as having negative values of  $m$  is simply a convenient shorthand notation; a particular planetary mode with a given positive value of  $m = m_*$  can, in principle, generate both an ILR with  $m = m_*$  and an OLR with  $m = -m_*$ . In practice, only the OLR is likely to fall within the main rings for  $m < 11$ . The reader should be careful not to confuse the negative values of  $m$  used here to denote OLRs with the retrograde planetary modes mentioned above. Where confusion might arise, we will use  $m_*$  to designate the (always positive) value of  $m$  for the normal mode under discussion.

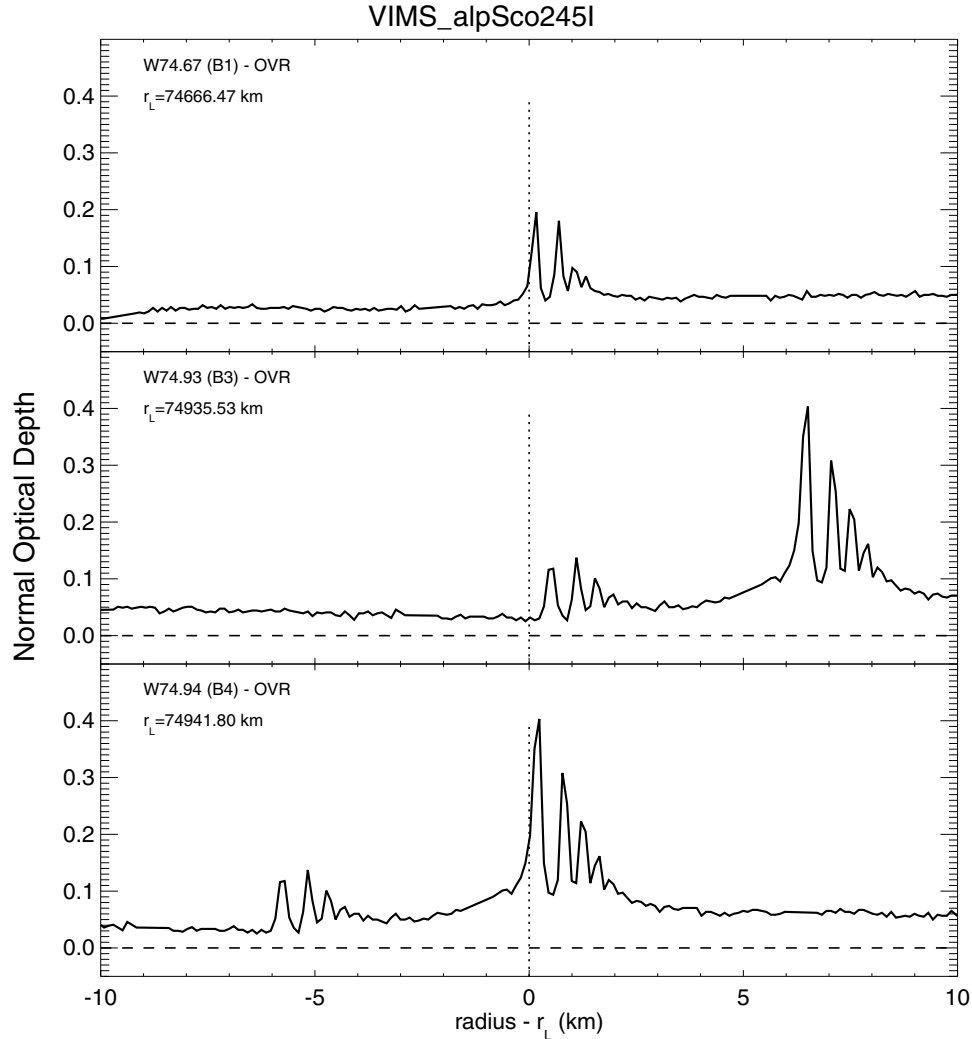


**Fig. 4.** Optical depth profiles of the inner three waves examined in this work, as observed in the ingress occultation of  $\alpha$  Scorpii on rev 245, on 15 October 2016, following the same format as Fig. 2. The radius scale here is approximate, due to the paucity of circular reference features.

where the wave phase is given by Hedman and Nicholson (2013)

$$\phi(r, \lambda, t) \simeq |m|(\lambda - \Omega_p t) + \phi_r(r). \quad (10)$$

$A(r)$  is a slowly-varying function of radius  $r$ , and  $f$  is either optical depth (for a density wave) or vertical slope (for a bending wave). The oscillatory function  $\phi_r(r)$  generates the radial profile of the wave, and for  $m \neq 1$  is given by the far-field expression (Hedman and Nicholson, 2013)

$$\phi(r) \simeq \frac{3(m-1)M_S(r-a_{\text{res}})^2}{4\pi\Sigma_0 a_{\text{res}}^4} + \phi_0. \quad (11)$$

Here,  $a_{\text{res}}$  is the resonant radius, where Eqs. (5) or (7) is satisfied,  $M_S$  is the mass of the planet, and  $\Sigma_0$  is the unperturbed surface mass density of the rings;  $\phi_0$  is a phase constant that depends on the orientation of the forcing mode in the planet at  $t = 0$ .

Our task in identifying a particular wave is to use multiple measurements of the waveform, at a range of times and inertial longitudes, to infer both the correct value of  $m$  and the pattern speed  $\Omega_p$ , using Eq. (10). Since the wave phase  $\phi$  varies rapidly with  $r$ , but the function  $\phi_r(r)$  should be the same at all azimuthal positions in the wave, this is most readily done by forming the differential phase between two observations of the same wave:

$$\delta\phi(r, \lambda, t) = \phi_i - \phi_j \simeq |m|(\delta\lambda - \Omega_p \delta t), \quad (12)$$

where  $\delta\lambda$  is the difference in longitude between the two observations and  $\delta t$  is the difference in time between them. In Section 4 we describe several methods whereby the wave phases can be determined observationally, and used to constrain the global characteristics of the waves.

### 3. Data

#### 3.1. Observations

As in Hedman and Nicholson (2013) and Hedman and Nicholson (2014), all of the data used in the present study come from stellar occultations observed by the Visual and Infrared Mapping Spectrometer (VIMS) instrument on Cassini (Brown, 2004). This data set has been described in the above papers, but for the present study has been extended to the end of the Cassini mission in 2017, on rev 292.<sup>2</sup> A total of 190 ring occultations have been observed, of which 158 have been measured for dynamical studies and 62 provide useful coverage of

<sup>2</sup> Cassini UVIS and RSS ring occultation data currently available on NASA's PDS Ring-Moon Systems Node are limited to 1 km resolution, which is inadequate for this investigation of sub-km wave structure. Once the higher-resolution UVIS and RSS results have been archived, it will be possible to include them in later studies.

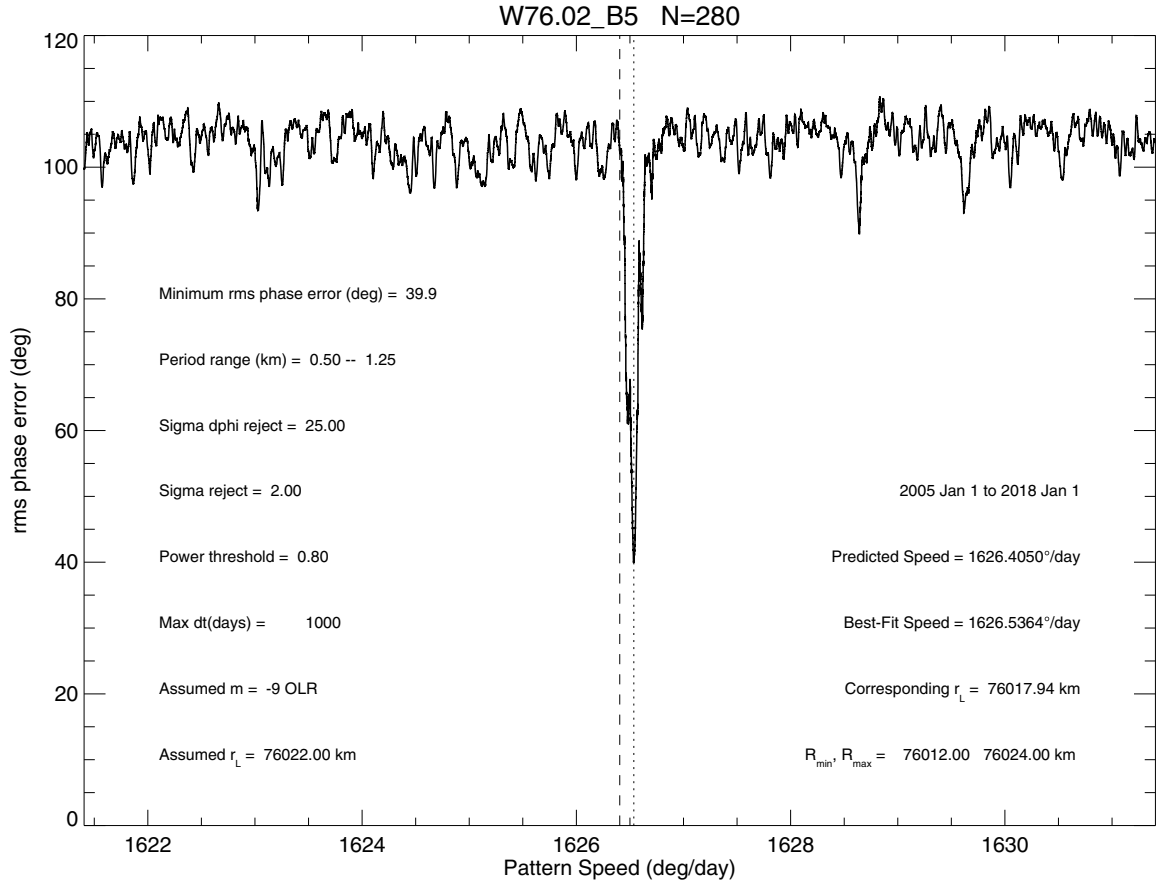


**Fig. 5.** The rms phase error  $\delta\phi_{\text{obs}} - \delta\phi_{\text{pred}}$  vs assumed pattern speed  $\Omega_p$  for OLR-type  $m = -9$  density wave W76.02 ((Baillié et al., 2011) feature B5), using 280 pairs of occultations and a maximum time difference of 1000 d. The best-fitting pattern speed is indicated by the dotted vertical line and the predicted value is indicated by the dashed vertical line, for an assumed resonance radius of 76022.0 km.

the inner C ring, spanning the period from March 2007 to September 2017, or 3900 d. Table 1 lists the data sets used, and key geometrical parameters. All of the data used here were obtained at a wavelength of  $2.92 \mu\text{m}$ , in order to minimize reflected and transmitted light from the rings. Radial resolution varies widely, being generally set by the instrument's sampling time combined with the projected velocity of the occultation point across the rings. Typical values are 250–500 m, but a few slow events have sampling intervals as low as 100 m and a few fast ones approach 1 km per sample. Time tags embedded in the data permit reconstruction of observation times to an accuracy of  $\sim 0.1$  ms, which is much higher than necessary for our purposes. This information is combined with knowledge of the reconstructed spacecraft trajectory (provided via SPICE files maintained by NAIF, the Navigation and Ancillary Information Facility at JPL (Acton, 1996; Acton et al., 2018)) and the stellar position<sup>3</sup> to determine the occultation point radius and inertial longitude for each sample, as described by French et al. (2010).

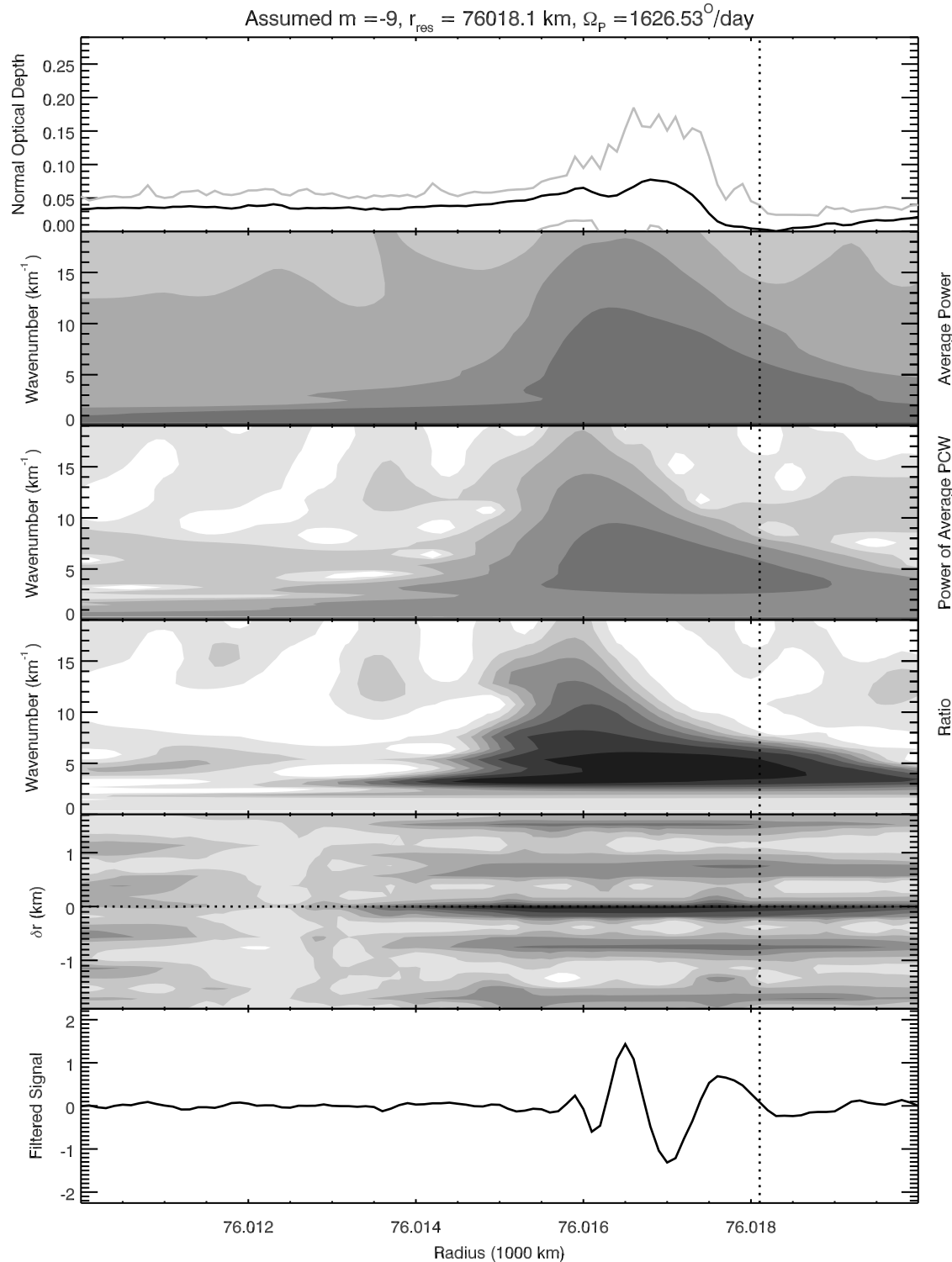
### 3.2. Selection of features

Our goal in this work is to exploit our improved knowledge of the absolute radius scale of the rings (French et al., 2017) to analyze several candidate waves in the inner C ring whose wavelengths have proven to be too short for previous investigations. To this end, we initially selected a list of six wavelike features, all interior to a radius of 77000 km, from the list of C ring waves compiled by Baillié et al. (2011), based on a survey of stellar occultation data obtained by Cassini's Ultraviolet

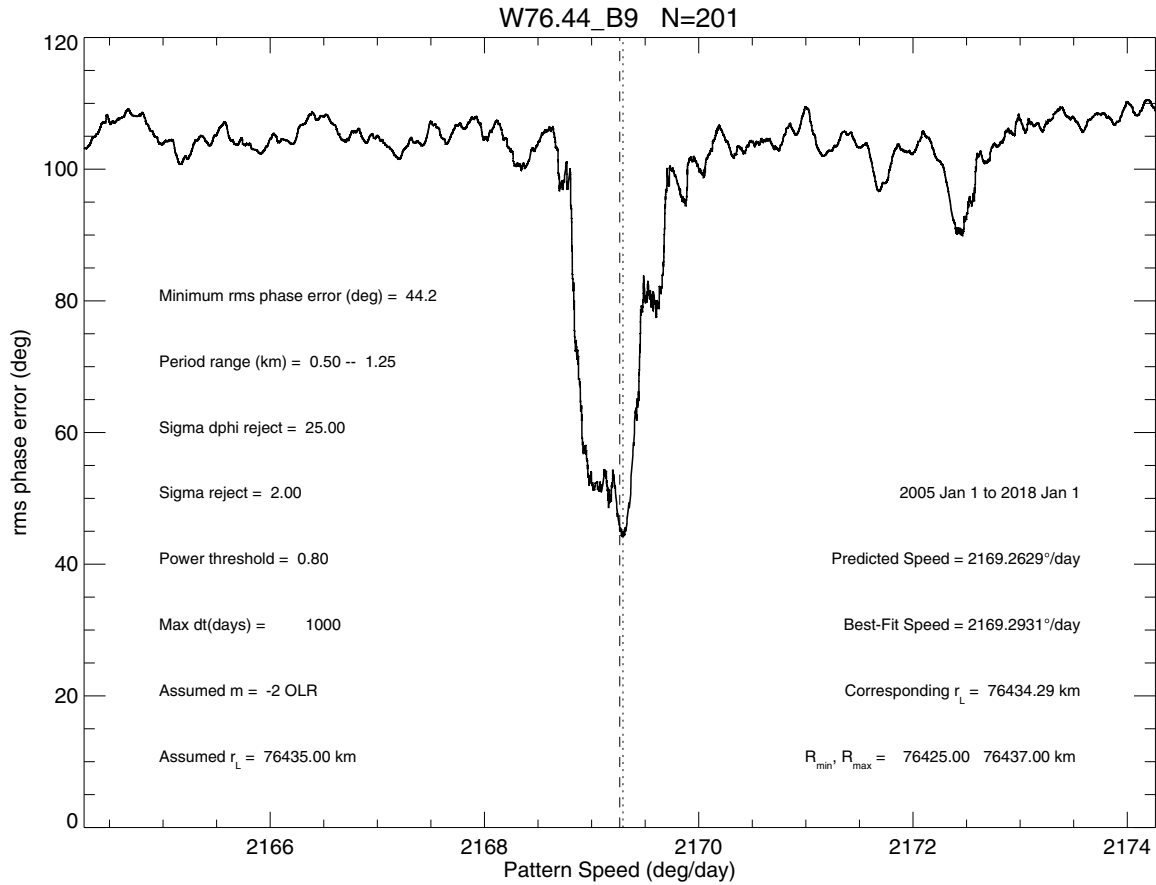
Imaging Spectrometer (UVIS). All were chosen based on preliminary inspections that showed detectable waves in at least some of the VIMS occultation profiles, with wavelengths of 1 km or greater; none has a pre-existing identification. We subsequently included an additional feature, designated W76.46, that does not appear in the catalog of Baillié et al. (2011) or in the lists compiled by Rosen et al. (1991) and Colwell et al. (2009), but which is quite evident in many VIMS occultations. Our list of features is presented in Table 2, along with other known or suspected waves in this region, with their *approximate* resonance radii, inferred direction of propagation — where available — and identifying codes from previous studies, if any. (The radii listed here are generally inferred resonance radii from Table 7 in Baillié et al. (2011), or otherwise our own visual estimates based on the best VIMS occultation profiles.) Also included in Table 2 are two additional wavelike features, designated B10 and B11 in the catalog of Baillié et al. (2011) and here denoted W76.53 and W76.73. Even the direction of propagation is uncertain for these waves. We thus have a total of nine unidentified waves to be analyzed.

Fig. 1 illustrates the region of interest in the inner C ring and the locations of the nine waves included in this study. There are only two known waves in this region driven by resonances with external satellites: the Mimas 4:1 ILR at a radius of 74890 km (Rosen et al., 1991; Hedman and Nicholson, 2014) and the Titan nodal ( $-1:0$ ) resonance at 77525 km (Rosen and Lissauer, 1988; Nicholson and Hedman, 2016). Both are clearly visible here. Also of interest is the eccentric Titan ringlet (Porco et al., 1984; Nicholson and Porco, 1988; Nicholson et al., 2014), located within the Colombo gap at a mean radius of  $\sim 77879$  km, and whose eccentricity is forced by the Titan apsidal ( $1:0$ ) resonance located at 77861 km. This strong Lindblad resonance is

<sup>3</sup> Derived from the Hipparcos catalog, but corrected for proper motion, parallax and stellar aberration at Saturn.



**Fig. 6.** Wavelet analysis of the OLR-type  $m = -9$  density wave W76.02 ((Baillié et al., 2011) feature B5), and construction of the phase-corrected mean wave profile. The upper panel shows the radial profile of the wave, the next three panels show the power of the wave as a function of wavenumber, as derived from wavelet analysis, the fifth panel compares the inferred resonance radius to the observed value, and the final panel shows the reconstructed waveform from the phase-corrected wavelet. See text for additional details.



**Fig. 7.** The rms phase error  $\delta\phi_{\text{obs}} - \delta\phi_{\text{pred}}$  vs assumed pattern speed  $\Omega_p$  for OLR-type  $m = -2$  density wave W74.43, ((Baillié et al., 2011) feature B9), using 201 pairs of occultations and a maximum time difference of 1000 d. The best-fitting pattern speed is indicated by the dotted vertical line and the predicted value is indicated by the dashed vertical line, for an assumed resonance radius of 76435.0 km.

responsible for the smaller but significant forced eccentricities seen on all sharp-edged features across this region (Nicholson et al., 2014).

### 3.3. Propagation direction

In Figs. 2 and 3 we show representative profiles of the nine wave features examined in this study, as observed in the occultations of  $\alpha$  Aurigae on rev 41 and  $\gamma$  Crucis on rev 187, plotted in order of increasing ring plane radius. These are among the highest-quality VIMS profiles of the inner C ring waves, and also provide snapshots of their appearance in the early and middle phases of the Cassini mission.

For seven of the waves, the decrease in radial wavelength as the wave propagates away from the driving resonance (cf. Eq. (11) above) is readily apparent. Features W76.02 (B5), W76.44 (B9), and W76.46 appear to propagate inwards, as expected for density waves driven at OLRs with saturnian normal modes. On the other hand, features W74.67 (B1), W74.93 (B3), W74.94 (B4) and W76.24 (B6) clearly propagate outwards, confirming the observations of Baillié et al. (2011). This suggests that these four waves may be identified either as density waves driven at ILRs with external satellites or as bending waves driven at OVRs. Since none of these features matches the location of a known satellite resonance, it appears more likely that some or all of these features represent a new category of wave, i.e., bending waves driven by out-of-plane perturbations due to saturnian normal modes. Our analysis of these waves confirms that this is indeed their most likely interpretation.

Fig. 4 shows profiles for three of these putative bending waves, from the occultation of  $\alpha$  Scorpii on rev 245. These are probably the highest-quality profiles obtained by VIMS for any of the inner C ring waves, but

unfortunately the occultation was interrupted by the star going behind Saturn at a radius of  $\sim 75000$  km, resulting in the loss of data for the remaining C ring waves. The outward propagation of all three waves is particularly clear in this figure from both the decrease in radial wavelength and the decrease in amplitude.

Figs. 2 and 3 also include two similar wavelike features in this part of the C ring, designated B10 and B11 in the catalog of Baillié et al. (2011), whose natures have so far not been ascertained. Baillié et al. (2011) concluded that B10 probably propagates inwards from a resonance located near 77539 km, but was unable to determine a direction for B11. We are in agreement with these statements, based on the visual inspection of a dozen or so high-quality VIMS occultation profiles, but suspect that the resonance radius for the former is closer to 77530 km.

## 4. Methods

Our method for determining the differential phase  $\delta\phi$  between two observations of a given wave is the same as that used previously by Hedman and Nicholson (2013) and Hedman and Nicholson (2014), and described in some detail by Hedman and Nicholson (2013). Briefly, it involves computing the local wavelet transform of each occultation profile, extracting the phase variations with radius  $\phi(r, \lambda, t)$ , and then forming the difference  $\delta\phi$  between pairs of occultations. This quantity is then compared with the predicted value of  $\delta\phi$  for trial values of  $m$  and  $\Omega_p$  from Eq. (12). Note that the pattern speed  $\Omega_p$  is not really a free parameter, as it must satisfy either Eq. (5) or Eq. (7), depending on whether a density or bending wave is involved. Of course, there is some *a priori* uncertainty in the resonant radius  $a_{\text{res}}$  at which  $n$ ,  $\dot{\omega}$  or  $\dot{\Omega}$  are

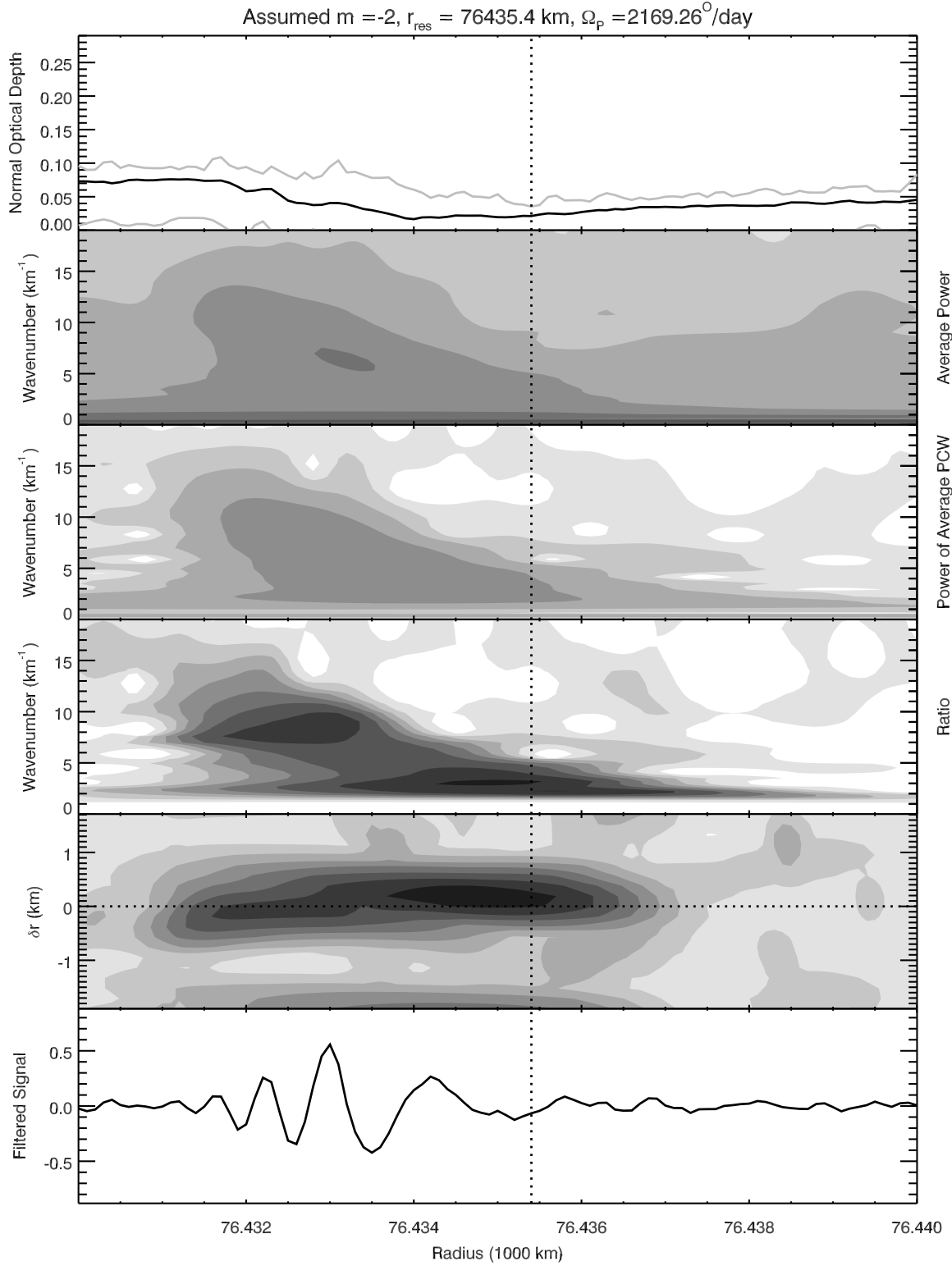


**Fig. 8.** Wavelet analysis of the OLR-type  $m = -2$  density wave W74.43, ((Baillié et al., 2011) feature B9), and construction of the phase-corrected mean wave profile. See caption for Fig. 6 and text for details.

evaluated, so in practice it is necessary to scan through a small range of values of  $\Omega_p$  for each wave.

Armed with both observed and predicted phase differences for many pairs of wave profiles, we can proceed in several ways. The simplest is to choose a small set of pairs of occultations, preferably ones with a small time difference  $\delta t$  so that  $\delta\phi$  is not overly sensitive to the assumed value of  $\Omega_p$ , and to specify a set of trial  $m$  values to identify

wavenumbers for which the observed and predicted phase differences match. While somewhat laborious, this approach does allow us to recognize multiple solutions and to identify individual measurements that may be corrupted in some fashion. This was the initial method adopted by Hedman and Nicholson (2013), using several chord occultations that provided two cuts across each wave. In the Appendix, we use this method as a test of our proposed mode identifications, and their

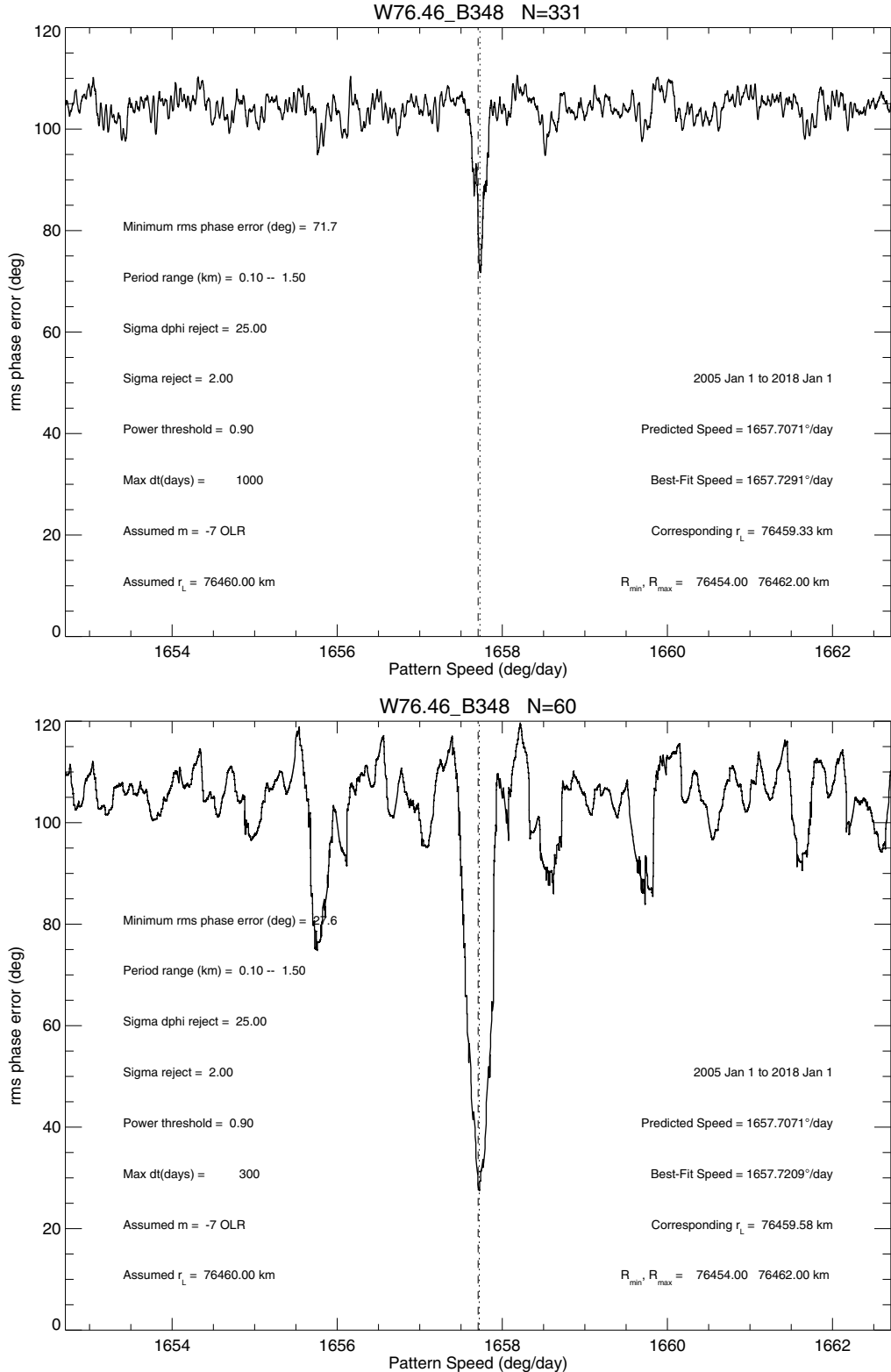


**Fig. 9.** The rms phase error  $\delta\phi_{\text{obs}} - \delta\phi_{\text{pred}}$  vs assumed pattern speed  $\Omega_p$ , for the candidate OLR-type density wave W76.46, using maximum time differences of 1000 d (upper panel) and 300 d (lower panel). Both fits are for  $m = -7$ , using 331 and 60 pairs of occultations, respectively. The fit in the lower panel includes only data from a small set of  $\gamma$  Cru occultations in 2008/9. The assumed resonance radius for both fits is 76460.0 km.

uniqueness.

A more sophisticated approach is to form all possible independent pairs of occultations and then to compute the residual phase  $\delta\phi_{\text{obs}} - \delta\phi_{\text{pred}}$  for each pair. The sum of these squared residuals is then minimized as a function of  $\Omega_p$ , for each trial value of  $m$ . This method

was employed by both Hedman and Nicholson (2013) and Hedman and Nicholson (2014), and will also be adopted here. One of the advantages of this approach is that it provides an accurate, objective estimate of the pattern speed.

Our third technique is to combine the wavelet transforms for all of

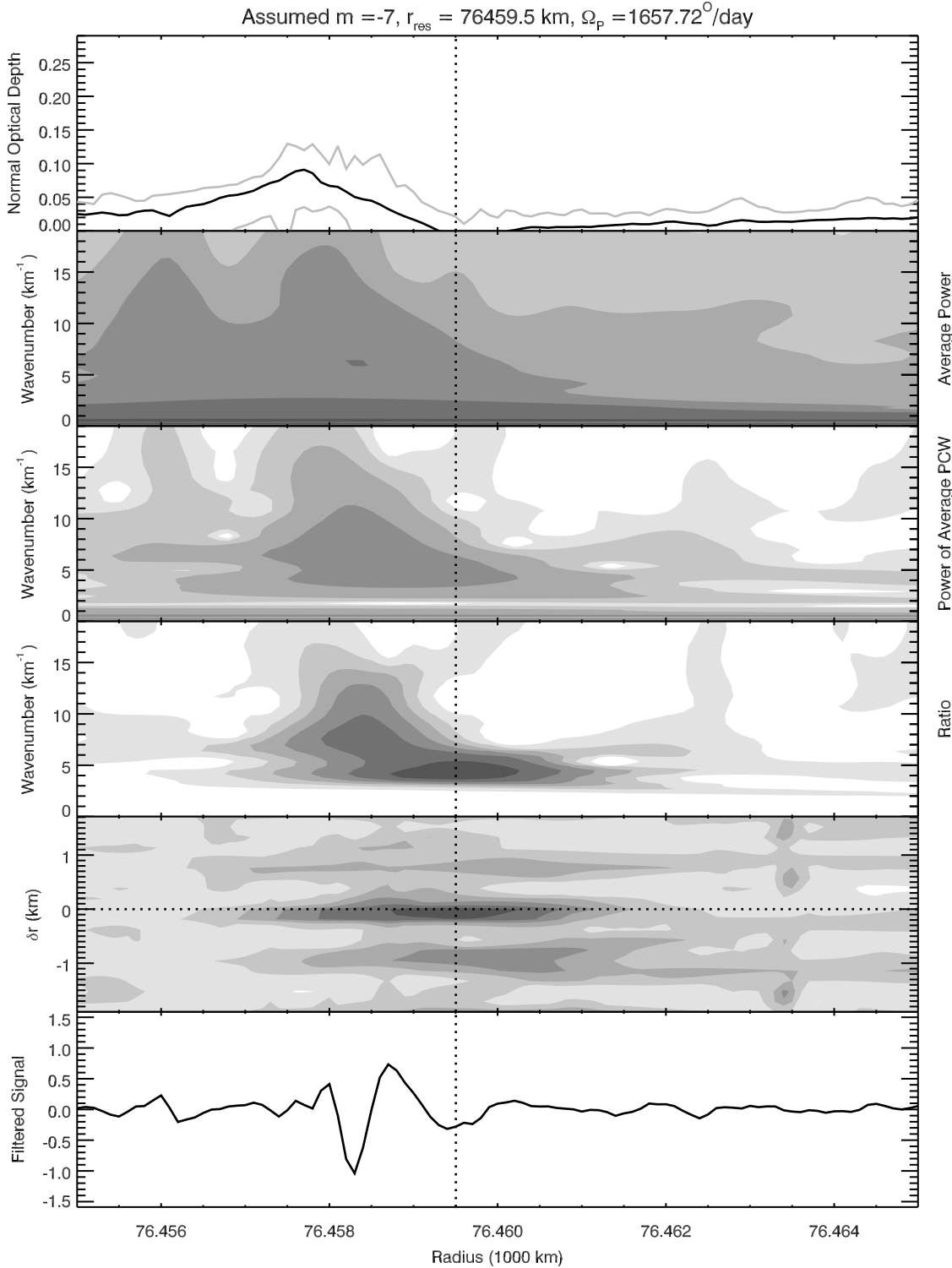


**Fig. 10.** Wavelet analysis of the candidate OLR-type  $m = -7$  density wave W76.46, and construction of the phase-corrected mean wave profile, using the full set of VIMS occultations. See caption for Fig. 6 and text for details.

the occultation profiles to construct an average phase-corrected wavelet for each wave, following the procedure described in detail by [Hedman and Nicholson \(2016\)](#). The essence of this method is that the phase of each individual wavelet is adjusted to a common epoch and longitude via Eq. (12), using assumed values of  $m$  and  $\Omega_p$ , before being added to a common wavelet profile. This phase-corrected profile is then examined to determine the trend in wavenumber with radius, for comparison with Eq. (11), and also used to reconstruct an average

radial profile of the wave. This approach is particularly effective for characterizing weak waves, especially those too weak to observe in most individual occultations.

The actual implementation of these procedures is more complicated, as it involves applying a filter to the raw wavelets in order to remove both very high (due to photometric noise) and very low (due to background variations) spatial frequencies, and averaging the phase differences over radius, weighted to emphasize the strongest parts of the

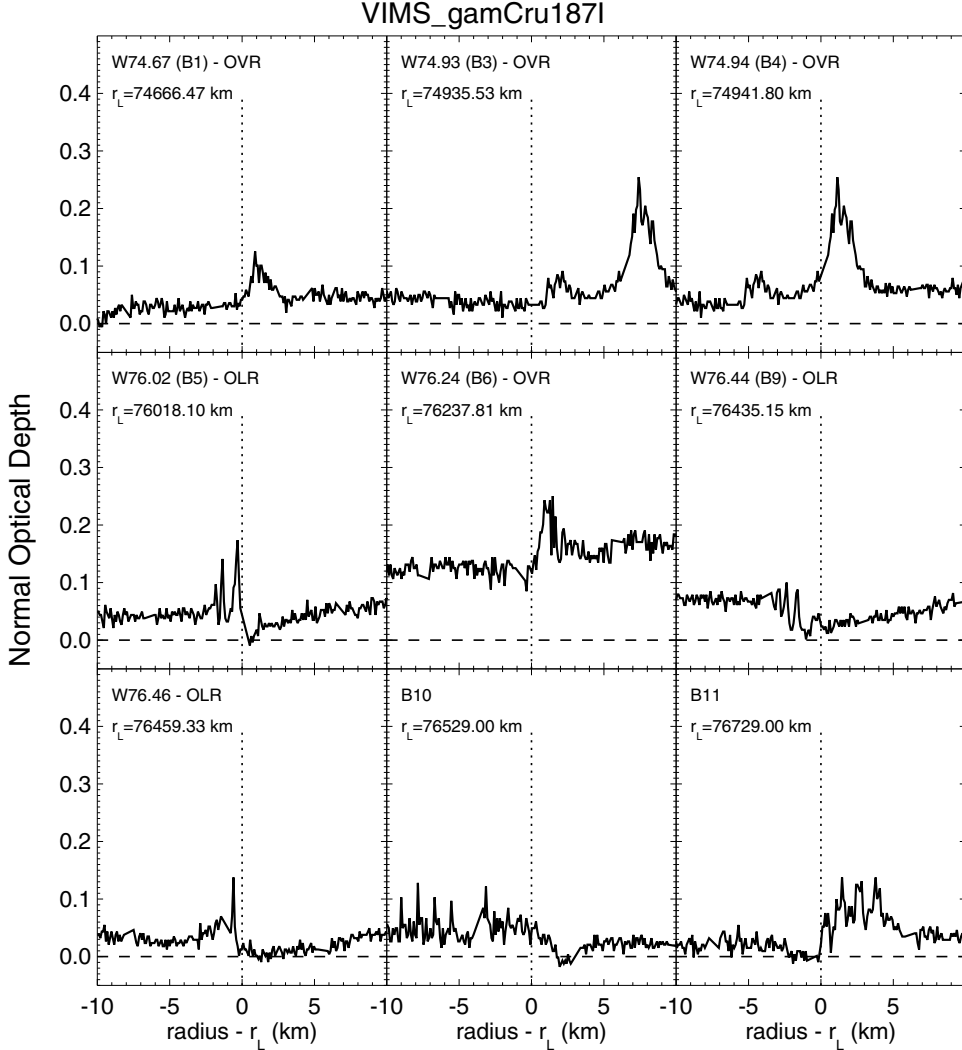


**Fig. 11.** Optical depth profiles of nine inner C ring waves obtained from the ingress occultation of  $\gamma$  Crucis on rev 187 on 22 April 2013, following the same format as Fig. 2. Compare the amplitudes of the putative bending (OVR) waves with those in the egress leg of the same occultation in Fig. 3.

wavetrains. For further details the interested reader is referred to [Hedman and Nicholson \(2013\)](#) and [Hedman and Nicholson \(2016\)](#).

An additional complication arises in the case of bending waves, whose appearance and apparent phase depend on the direction of observation as well as the wave itself. A convenient way to capture this dependence is to introduce the effective elevation angle of the star, denoted  $B_{\text{eff}}$  and defined by ([Gresh et al., 1986](#); [Nicholson et al., 1990](#))

$$\tan B_{\text{eff}} = \frac{\tan B_*}{\cos(\lambda - \lambda_*)}, \quad (13)$$

where  $B_*$  is the elevation angle of the occulted star above the ring plane and  $\lambda_*$  is the star's inertial longitude. A segment of ring of normal optical depth  $\tau_n$  that is inclined with respect to the mean ring plane by a slope  $s = dz/dr$  will appear to have an optical depth

$$\tau \simeq \tau_n(1 - \beta s)/\sin B_*, \quad (14)$$

where  $\beta = (\tan B_{\text{eff}})^{-1}$  and we have assumed that  $s \ll \tan B_{\text{eff}}$ . A bending wave is visible in an occultation profile by virtue of its variable slope, which translates into a corresponding variation in the line-of-sight optical depth  $\tau$ . Eq. (14) shows that the sign of the change in  $\tau$  is determined by the sign of the geometric parameter  $\beta$  as well as the sign of the intrinsic slope  $s$ . We account for this dependence in our phase-comparison code for bending waves by adding  $180^\circ$  to the observed wave phase whenever  $\beta < 0$ .

For low-frequency waves, such as those where  $\sigma_0$  is large or  $|m - 1|$  is small, it is relatively straightforward to estimate the wave phase to within  $10^\circ$  or so. But for larger values of  $|m|$ , or in parts of the rings where  $\sigma_0$  is small, such as the inner C ring, this becomes a significant challenge. This is, in fact, what led ([Hedman and Nicholson, 2013](#)) and ([Hedman and Nicholson, 2014](#)) to exclude waves in this region from their studies. This problem is exacerbated by errors in the absolute radius scale of the occultation profiles. Many of the C ring waves have radial wavelengths of only a few km, or even less, whereas systematic errors in the geometric reconstruction of stellar and radio occultations are of order 1 km, due to uncertainties in the reconstructed Cassini trajectory, which can in turn lead to phase errors of as much as  $180^\circ$ .

But as part of an attempt to refine the absolute radial scale of the rings, as well as Saturn's pole direction, ([French et al., 2017](#)) recently used a very large suite of Cassini occultation measurements to identify circular ring features (sharp gap and ring edges, narrow ringlets, etc.), and determined their absolute radii to an accuracy of  $\sim 250$  m. As part of this work, it was necessary to determine corrections to the spacecraft trajectory at the time of each occultation. These corrections are now available for almost all Cassini ring stellar and radio occultations, and are believed to be accurate to  $\sim 150$  m in most cases. After applying these corrections to the VIMS occultation profiles, we have a self-consistent set of ring measurements with internal errors of  $\sim 150$  m and absolute errors of  $\sim 250$  m. The former estimate is borne out by fits to

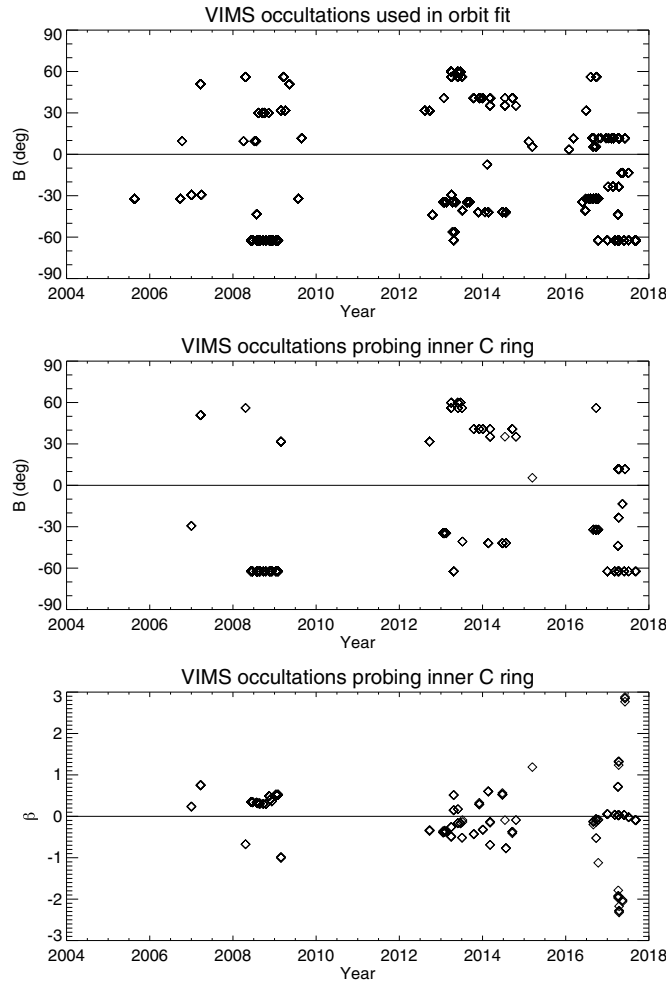


**Fig. 12.** The distribution of VIMS ring stellar occultations as a function of date, stellar elevation angle  $B_*$  and the vertical structure factor  $\beta = (\tan B_{\text{eff}})^{-1}$ . The upper panel shows all occultations included in the ring geometry model of French et al. (2017), while the middle and lower panels show only those that covered the radial range interior to 77000 km. Long gaps in the record in 2005/6, 2007/8, 2010–2012 and in 2015 represent periods when the spacecraft was on near-equatorial orbits unfavorable to observing ring observations. Dense clumps of observations at  $B_* = -62.3^\circ$  indicate occultations of  $\gamma$  Crucis, while those at  $B_* = +11.7^\circ$  involve  $\alpha$  Ori.

over 60 nominally circular ring features, many of which have RMS residuals of this order.

A final correction that we have found to be essential in the inner C ring is due to the widespread effects of the Titan apsidal resonance, which introduces measurable forced eccentricities into all ring particle orbits within  $\sim 3500$  km of the resonant radius of 77861 km (Nicholson et al., 2014). Fortunately, the geometry is simple, with forced periapses aligned with Titan interior to the resonance and anti-aligned with Titan exterior to the resonance. The forced radial displacement at longitude  $\lambda$  is given by the approximate expression

$$\Delta r = 382 \frac{\cos(\lambda - \lambda_T)}{a - a_{\text{res}}} \text{ km}, \quad (15)$$

where  $\lambda_T$  is the longitude of Titan at the time of the observation and  $a - a_{\text{res}}$  is given in km. We subtract this correction, which for the waves in question can amount to as much as 0.25 km, from the observed occultation radii to convert them to semimajor axis. This is a substantial fraction of the wavelength of some of the detected waves, and must be taken into account for reliable wave identification.

## 5. Density waves

We turn first to the three inward-propagating waves, features W76.02, W76.44 (Baillié's B5 and B9, respectively), and W76.46, which we suspect to be density waves similar to those studied previously (Hedman and Nicholson, 2013; 2014). Overall, we have  $\sim 60$  VIMS occultation profiles spanning the period 2007–2017, corresponding to a maximum of  $\sim 1800$  pairs for which phase differences  $\delta\phi$  can be calculated. In practice, however, not every occultation profile yields a satisfactory wavelet phase for each feature of interest, and the typical number of usable pairs is under 1000. This may reflect the fact that, as seen in Figs. 2 and 3, only 2 and 3 peaks in optical depth are visible for these two waves, even in the best profiles.

We have carried out multiple fits for each wave, using various cutoff levels for the uncertainty in the mean phase of individual occultations  $\sigma_{\text{phase}}$ , and the maximum time difference between occultation pairs  $\delta t_{\text{max}}$ . Typically, we set  $\sigma_{\text{phase}} = 25^\circ$  and  $\delta t_{\text{max}} = 1000$  or 4000 d. We also adjusted the range of spatial frequencies used to compute the average wavelet phase, trimming off the highest frequencies (which are dominated by noise) and also the lowest (dominated by background variations in optical depth). Most of our final fits only include spatial periods between a minimum of 0.3–0.5 km and a maximum of 1.0–1.25 km. All of our final fit results are summarized in Table 3 and illustrated in Figs. 5–10.

### 5.1. W76.02 (B5) OLR wave

Catalogued as feature B5 by Baillié et al. (2011), this wave is well-fitted by a density wave with  $m = -9$  (i.e., an OLR-type wave). If we restrict  $\delta t_{\text{max}}$  to 1000 days, we have 280 surviving occultation pairs and the best-fitting pattern speed is  $1626.54^\circ \text{ d}^{-1}$ . The minimum in the rms phase residuals is  $39.9^\circ$  and there are no other minima in the residuals below  $80^\circ$  within  $\pm 20^\circ \text{ d}^{-1}$  of the expected value of  $\Omega_p$ . The resonance radius corresponding to the best-fitting pattern speed, calculated using Eq. (5), is 76017.94 km, which agrees tolerably well with Baillié et al. (2011)'s estimate of 76022 km. A plot of the rms phase residuals vs pattern speed is shown in Fig. 5.

If we now extend  $\delta t_{\text{max}}$  to 4000 days, so that all possible pairs of VIMS occultations are included, we have 839 occultation pairs with measurable values of  $\delta\phi$  and the best-fitting pattern speed is reduced slightly to  $1626.53^\circ \text{ d}^{-1}$ , with the minimum rms phase residual remaining essentially unchanged at  $41.3^\circ$ . This consistency in pattern speed and overall rms residuals suggests that the wave has remained remarkably stable in its primary characteristics over the 10 yr duration of the Cassini-VIMS data set. During this period, the pattern has made over 16,000 rotations around the planet and the 9 spiral arms have crossed a given longitude almost 150,000 times, with a phase jitter of  $< 45^\circ$ .

We can obtain a better picture of the wave structure by constructing the average phase-corrected wavelet for the wave, as shown in Fig. 6. The top panel shows the mean normal optical depth of the wave, along with the range of optical depths among the various profiles used to produce the phase-corrected wavelet reconstruction of the wave. The second panel shows the average wavelet power as a function of radius and wavenumber, without any phase corrections applied to the wavelet power of individual occultation profiles. A broad diagonal ridge with negative slope suggests that the wavenumber increases to the left (i.e., that the wave propagates inward). This is somewhat more evident in the third panel, which shows the power of the average phase-corrected wavelet (PCW), assuming  $m = -9$  and resonance radius  $a_{\text{res}} = 76018.1$  km (marked by a vertical dotted line). (The powers are plotted using the same logarithmic stretch). The fourth panel shows the ratio of the above powers, using a linear gray scale, highlighting the improvement in the wave detection by using the phase-corrected wavelet rather than simply co-adding the wavelet power. The fifth panel shows the peak value of the power ratio as a function of radius and assumed pattern speed,

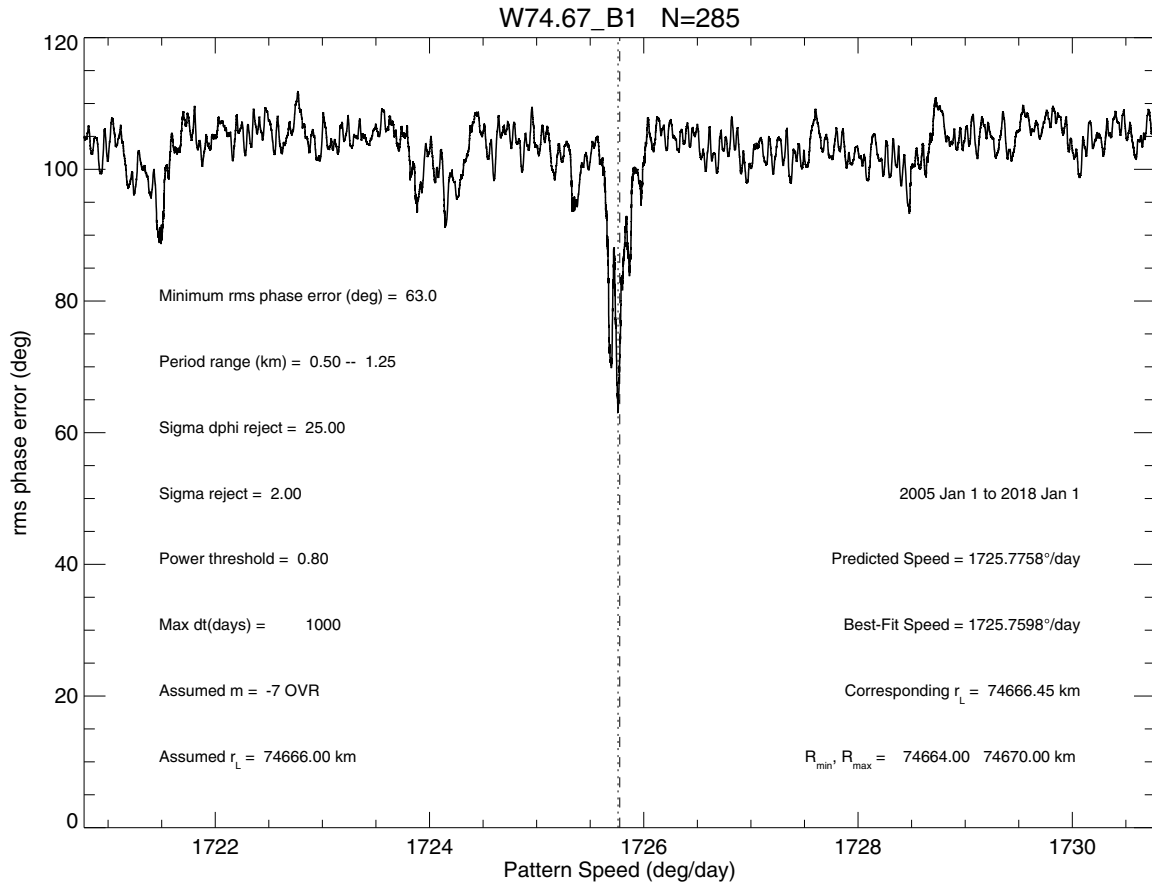


**Fig. 13.** The rms phase error  $\delta\phi_{\text{obs}} - \delta\phi_{\text{pred}}$  vs assumed wavenumber  $m = -7$  and pattern speed  $\Omega_p$ , for bending wave W74.67 (B1), using a maximum time difference of 1000 d and 285 pairs of occultations.

parameterized as a displacement  $\delta r$  from the expected resonance location, marked with a horizontal dotted line. The dark gray band near  $\delta r = 0$  km is a strong indication that the assumed resonance radius and pattern speed are correct for this wave. The fainter bands at  $\pm 0.7$  km represent aliased solutions, and correspond to shifts  $\pm 0.024^\circ \text{d}^{-1}$  in pattern speed, or 1 wave cycle (i.e.,  $360^\circ/m$ ) in  $\sim 1800$  d, which is approximately the time between the two large groups of occultations used in this analysis. The bottom panel shows the phase-corrected mean wave profile, with wavelength decreasing to the left, as expected for an inward-propagating wave.

### 5.2. W76.44 (B9) OLR wave

Catalogued as feature B9 by Baillié et al. (2011), this wave is well-fitted by a density wave with  $m = -2$  (i.e., another OLR-type wave). If we restrict  $\delta t_{\text{max}}$  to 1000 days, we have 201 occultation pairs and the best-fitting pattern speed is  $2169.29^\circ \text{d}^{-1}$ . The minimum in the rms phase residuals is  $44^\circ$ . The resonance radius corresponding to this pattern speed, calculated using Eq. (5), is 76434.3 km, which agrees quite well with (Baillié et al., 2011)'s estimate of 76435 km. A plot of the rms phase residuals vs pattern speed is shown in Fig. 7.

If we now extend  $\delta t_{\text{max}}$  to 4000 days, we have 576 occultation pairs and the best-fitting pattern speed is reduced slightly to  $2169.26^\circ \text{d}^{-1}$ , with a minimum rms phase residual of  $46^\circ$ . But in this case there are several closely-spaced minima, separated by intervals of  $\sim 0.12^\circ \text{d}^{-1}$ . This corresponds to one extra cycle (i.e.,  $360^\circ/m$ ) of the 2-armed spiral pattern in a period of  $\sim 4.1$  years, or a shift in the resonance radius of 2.8 km. Inspection of the temporal distribution of the available data (see Fig. 12 below) shows that this is almost certainly due to the lengthy gaps in our data set in 2010–12 and 2015, which

result in three major groups of data separated by intervals of  $\sim 4$  years.

The identity of this wave is supported using the phase-corrected wavelet approach to characterize the wave properties, as shown in Fig. 8. The diagonal band in the wavelet power spectrum (panels 2–4) indicates an inward-propagating wave, and the dark horizontal band near  $\delta r = 0$  confirms the consistency of the assumed pattern speed and resonance radius. The reconstructed wavelet in the bottom panel shows multiple sub-km scale wave crests, detectable by virtue of the very accurate absolute radius scale used to align the observations.

### 5.3. W76.46 OLR wave

Experiments with a range of assumed values of  $m$  show that this apparently inward-propagating wave is well-fitted by a density wave with  $m = -7$  (i.e., it is indeed another OLR-type wave). If we set  $\delta t_{\text{max}}$  to 1000 days, as for the above fits, we have 331 occultation pairs but the minimum in the rms phase residuals is a rather poor  $72^\circ$ . The resonance radius corresponding to the best-fitting pattern speed of  $1657.73^\circ \text{d}^{-1}$ , calculated using Eq. (5), is 76459.33 km agreeing quite well with our eyeball estimate of 76460 km.

On the assumption that the substantial phase residuals might reflect the extreme sensitivity of the fits to such a high-frequency wave to remaining small trajectory errors, or to noise in some data sets, we repeated the fit using only the 17 very high-quality occultations of  $\gamma$  Cru in 2008/9. While this reduces the number of available occultation pairs to 60, the fit is much improved, with a minimum rms phase residual of  $28^\circ$ . The best-fit pattern speed is essentially unchanged.

Plots of the rms phase residuals vs pattern speed for both fits are shown in Fig. 9, and the corresponding wavelet reconstruction results are shown in Fig. 10. Again the fifth panel shows weaker side lobes, this

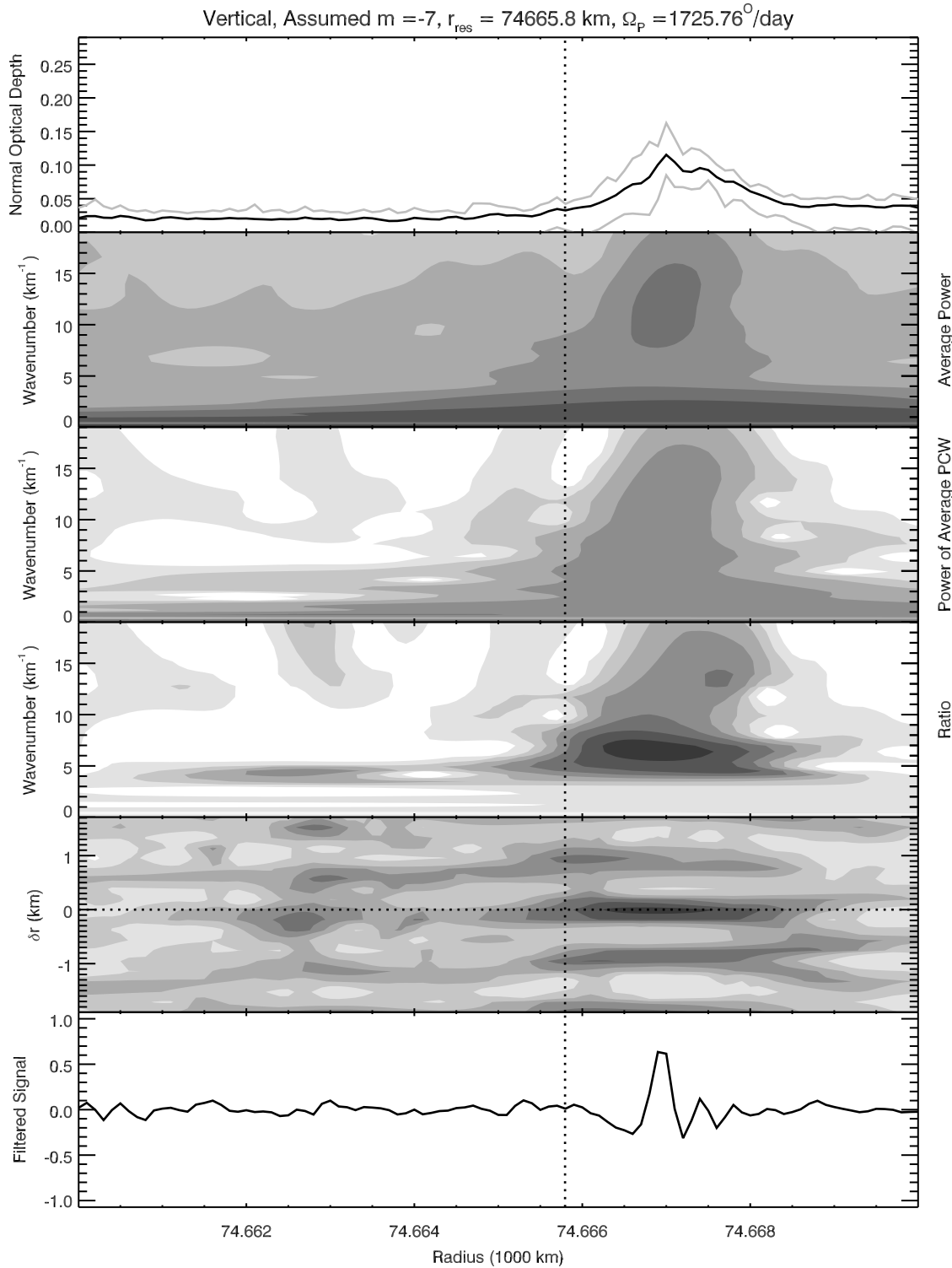


**Fig. 14.** Wavelet analysis of the OVR-type  $m = -7$  bending wave W74.67 (B1), and construction of the phase-corrected mean wave profile. See caption for Fig. 6 and text for details. Note that, unlike Figs. 6, 8 and 10, the diagonal ridge in wavelet power as a function of wavenumber increases with radius, indicative of an outward-propagating wave.

time at  $\delta r \approx \pm 1$  km, suggesting the possibility of alternate fits with values of  $\Omega_p$  differing by  $\pm 0.028^\circ \text{ d}^{-1}$  from the best-fitting model, or one extra cycle (i.e.,  $360^\circ/m$ ) in  $\sim 1800$  d. Although not quite as robust as the fits to the W76.02 and W7.44 waves above, we consider the identification of this feature as an OLR-type density wave with  $m = -7$  to be fairly secure, but subject to future confirmation using a larger data set and an improved Cassini trajectory.

## 6. Bending waves

Turning now to the four outward-propagating waves W74.67, W74.93, W74.94 and W76.24 (Baillié's features B1, B3, B4 and B6, respectively), we must consider the likelihood that these are bending waves rather than density waves. We allow for this by making two changes to our fits: the predicted pattern speeds are calculated using

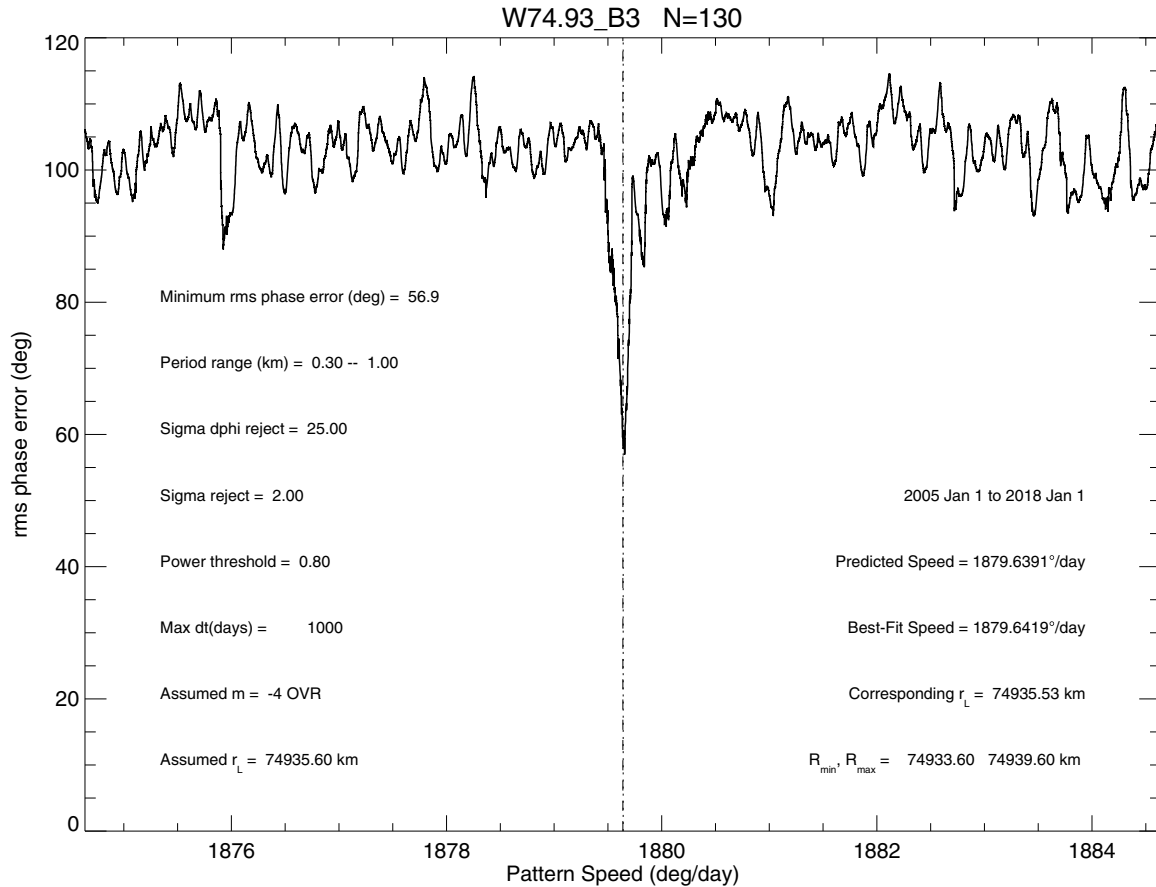


**Fig. 15.** The rms phase error  $\delta\phi_{\text{obs}} - \delta\phi_{\text{pred}}$  vs assumed wavenumber  $m = -4$  and pattern speed  $\Omega_p$ , for bending wave W74.93 (B3), using a maximum time difference of 1000 d and 130 pairs of occultations, with an assumed resonance radius of 74935.6 km.

Eq. (7) rather than Eq. (5), and the parameter  $\beta = (\tan B_{\text{eff}})^{-1}$ , calculated using Eq. (13), is used to adjust the observed wavelet phases as described in Section 4 above, i.e., by adding  $180^\circ$  to the observed wave phase whenever  $\beta < 0$ . This phase shift was also incorporated in the phase-corrected wavelet analyses.

In all other respects, the bending wave fits are identical to the density wave fits described above, and the final fit results are again summarized in Table 3 and illustrated in Figs. 13–20 below.

In addition to the apparent phase of bending waves being sensitive to the sign of  $\beta$ , occultations with larger absolute values of  $\beta$  are much more sensitive to vertical structure than are those with smaller  $|\beta|$ . This is illustrated in Fig. 11, which shows our nine inner C ring waves as observed on the ingress leg of the same occultation shown in Fig. 3 (i.e.,  $\gamma$  Crucis, rev 187), but at a different longitude. In Fig. 3 we have  $\beta = 0.51$  and the amplitudes of the four putative bending waves are quite strong, whereas in Fig. 11 we have  $\beta = 0.16$  and these particular waves are much more muted. Note that the three density waves, however, are independent of  $\beta$  and look essentially the same at ingress and egress, as expected. Such comparisons provide valuable independent evidence that certain features are indeed bending waves, as we had initially suspected from their direction of propagation.

Fig. 12 shows the distribution over the Cassini mission of VIMS ring occultations as functions of the stellar elevation angle  $B_*$  and the vertical structure factor  $\beta = (\tan B_{\text{eff}})^{-1}$ . Rather surprisingly, all of the occultations that probed the inner C ring with very high sensitivity to inclined features were observed in the last year of the mission.

### 6.1. W74.67 (B1) OVR wave

Catalogued as feature B1 by Baillié et al. (2011), this wave is well-fitted by a bending wave with  $m = -7$  (i.e., it is an OVR-type wave). If we restrict  $\delta t_{\text{max}}$  to 1000 days, we have 285 occultation pairs and the best-fitting pattern speed is  $1725.76^\circ \text{d}^{-1}$ . The minimum in the rms phase residuals is  $63^\circ$ , somewhat poorer than the fits for B5 and B9 above. The resonance radius corresponding to this pattern speed, calculated using Eq. (7), is 74666.45 km, which agrees well with (Baillié et al., 2011)'s estimate of 74666 km. A plot of the rms phase residuals vs pattern speed is shown in Fig. 13.

If we now extend  $\delta t_{\text{max}}$  to 4000 days, we have 753 occultation pairs but the best-fitting pattern speed is unchanged, with a slightly larger minimum rms phase residual of  $67^\circ$ . Again there are several closely-spaced minima, in this case separated by intervals of  $\sim 0.03^\circ \text{d}^{-1}$ , corresponding to one extra cycle of the 7-armed spiral pattern in a period of  $\sim 4.7$  years. The corresponding shift in the resonance radius is 0.9 km.

The identity of this wave is supported using the phase-corrected wavelet approach to characterize the wave properties, as shown in Fig. 14. Here, the diagonal ridge in wavelet power as a function of wavenumber increase with radius, indicative of an outward-propagating wave. The dark band in the fifth panel near  $\delta r = 0$  confirms the consistency of the assumed pattern speed and the corresponding resonance radius for this OVR-type wave. But again the fifth panel shows weaker side lobes, this time at  $\delta r \simeq \pm 0.9$  km, suggesting the

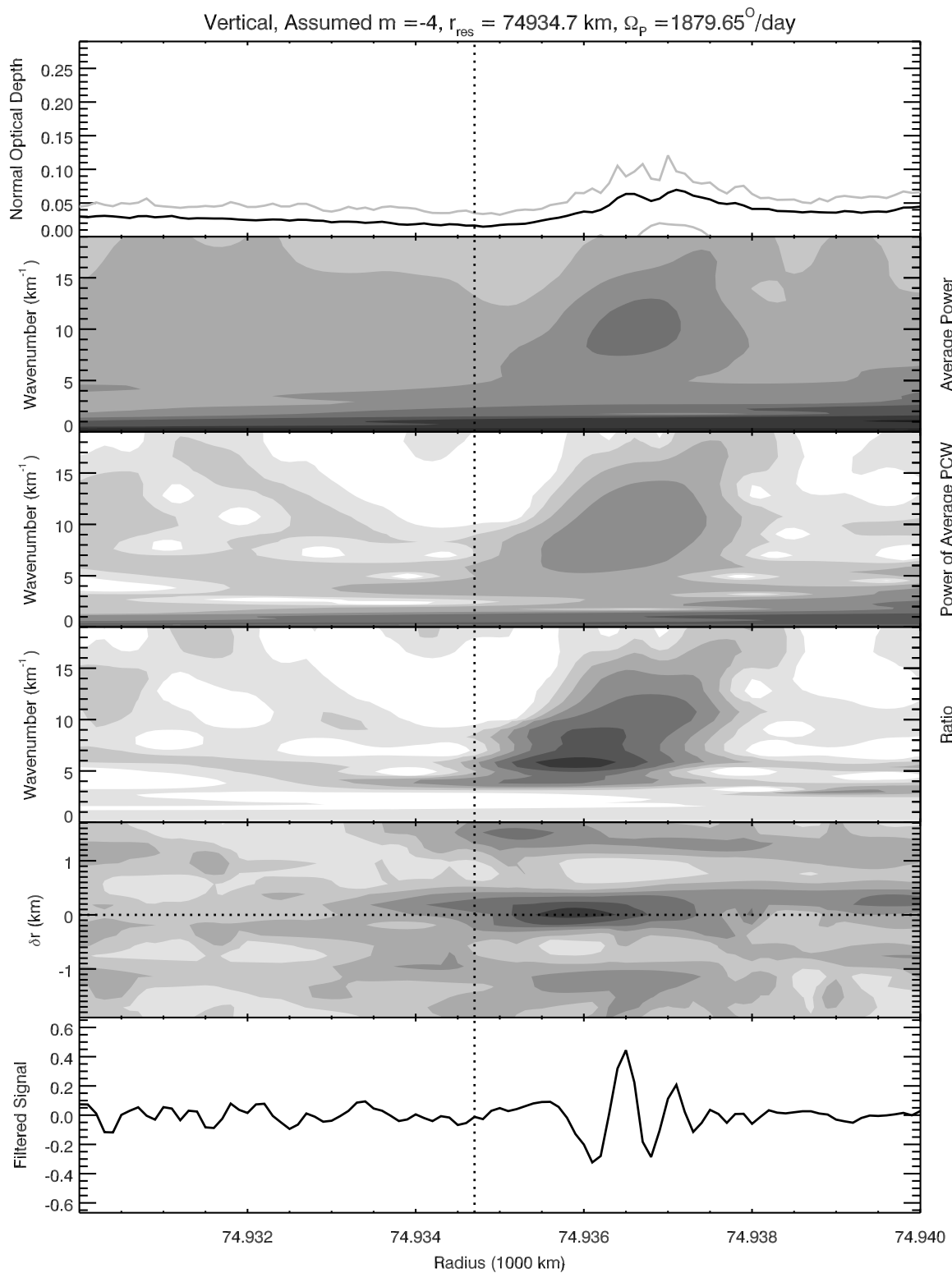


**Fig. 16.** Wavelet analysis of the OVR-type  $m = -4$  bending wave W74.93 (B3), and construction of the phase-corrected mean wave profile. See caption for Fig. 6 and text for details.

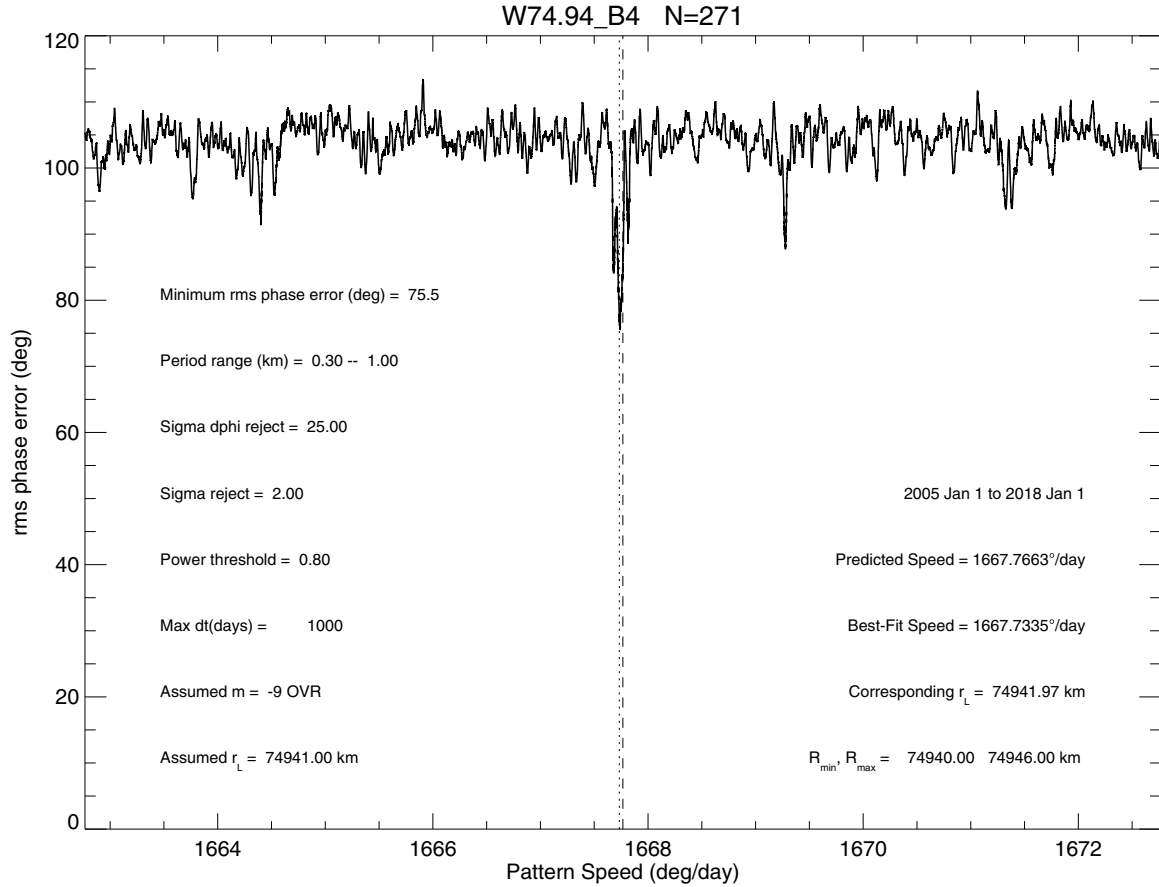


**Fig. 17.** The rms phase error  $\delta\phi_{\text{obs}} - \delta\phi_{\text{pred}}$  vs assumed pattern speed  $\Omega_p$ , for bending wave W74.94 (B4), using a maximum time difference of 1000 d and 271 pairs of occultations, for an assumed wavenumber  $m = -9$  resonance radius of 74941.0 km.

possibility of alternate fits with values of  $\Omega_p$  differing by  $\pm 0.025^\circ \text{ d}^{-1}$  from the best-fitting model, or 1 extra cycle in  $\sim 2000$  d.

## 6.2. W74.93 (B3) OVR wave

Catalogued as feature B3 by Baillié et al. (2011), this wave is well-fitted by a bending wave with  $m = -4$  (i.e., it is also an OVR-type wave). If we restrict  $\delta t_{\max}$  to 1000 days, we have 130 occultation pairs and the best-fitting pattern speed is  $1879.64^\circ \text{ d}^{-1}$ . The minimum in the rms phase residuals is  $57^\circ$ , similar to that for feature B1. The resonance radius corresponding to the pattern speed, calculated using Eq. (7), is 74935.53 km, which agrees fairly well with Baillié et al. (2011)'s estimate of 74933 km.<sup>4</sup> A plot of the rms phase residuals vs pattern speed is shown in Fig. 15.

If we now extend  $\delta t_{\max}$  to 4000 days, we have 371 occultation pairs but the best-fitting pattern speed is unchanged, with a slightly larger minimum rms phase residual of  $61^\circ$ . There are two closely-spaced minima, separated by  $\sim 0.06^\circ \text{ d}^{-1}$ , corresponding to one extra cycle of the 4-armed spiral pattern in a period of  $\sim 4.1$  years. The corresponding shift in the resonance radius is 1.6 km.

The identity of this wave is supported using the phase-corrected wavelet approach to characterize the wave properties, as shown in Fig. 16. Again, the diagonal ridge in the wavelet power spectrum indicates an outward-propagating wave, as seen also in the reconstructed wavelet profile in the bottom panel. Weak side lobes in the fifth panel at  $\delta r \simeq \pm 1.3$  km suggest the possibility of alternate fits with values of  $\Omega_p$  differing by  $\pm 0.028^\circ \text{ d}^{-1}$  from the best-fitting model, or 1 extra cycle in

$\sim 3500$  d.

## 6.3. W74.94 OVR wave

Catalogued as feature B4 by Baillié et al. (2011), and wave ‘b’ by Rosen et al. (1991), this wave is located only 6 km exterior to feature B3, but is notably stronger. It is well-fitted by a bending wave with  $m = -9$  (i.e., it is also an OVR-type wave). If we restrict  $\delta t_{\max}$  to 1000 days, we have 271 occultation pairs and the best-fitting pattern speed is  $1667.73^\circ \text{ d}^{-1}$ . The minimum in the rms phase residuals is a relatively poor  $75^\circ$ . The resonance radius corresponding to the pattern speed, calculated using Eq. (7), is 74941.97 km, which again agrees fairly well with Baillié et al. (2011)'s estimate of 74939 km. A plot of the rms phase residuals vs pattern speed is shown in Fig. 17.

If we now extend  $\delta t_{\max}$  to 4000 days, we have 741 occultation pairs but the best-fitting pattern speed is almost unchanged at  $1667.74^\circ \text{ d}^{-1}$ , with a slightly smaller minimum rms phase residual of  $71^\circ$ . There are again several closely-spaced minima, separated by  $\sim 0.03^\circ \text{ d}^{-1}$ , corresponding to one extra cycle of the 9-armed spiral pattern in a period of  $\sim 3.7$  years. The corresponding shift in the resonance radius is 0.9 km. One might ask why the rms residuals for the fits to this wave are significantly larger than those obtained for the clearly weaker W74.67 and W74.93 waves. One possibility is that the larger value of  $m$  here means that the radial wavelengths are smaller, which makes our phase estimates even more sensitive to small trajectory errors. The larger  $m$  also implies a greater sensitivity of the model phases to the assumed pattern speed. A third possibility is that the location of the wave atop a local maximum in optical depth (see Fig. 2) results in a distortion of the usual dispersion relation.

The identity of this wave is supported using the phase-corrected

<sup>4</sup> Allowing for a typo in their Table 7, which lists a value of 74923 km.

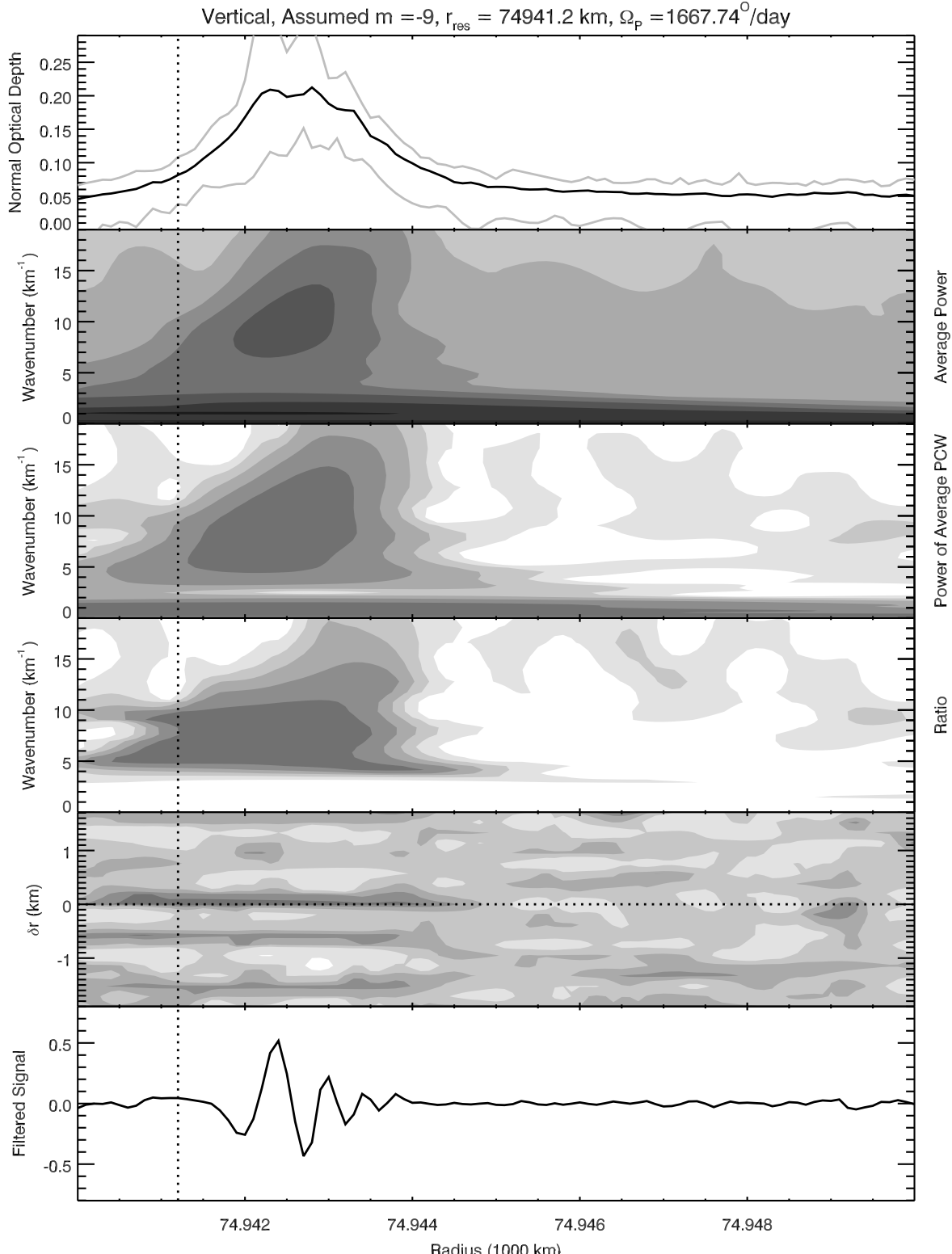


**Fig. 18.** Wavelet analysis of the OVR-type  $m = -9$  bending wave W74.94 (B4), and construction of the phase-corrected mean wave profile. See caption for Fig. 6 and text for details.

wavelet approach to characterize the wave properties, as shown in Fig. 18. In this case, the linear diagonal ridge in wavelet power with increasing wavenumber is quite evident in panels 2–4, and the reconstructed wavelet in the bottom panel clearly shows an outward-propagating wave.

#### 6.4. W76.24 OVR wave

Catalogued as feature B6 by Baillié et al. (2011), this wave is well-fitted by a bending wave with  $m = -8$  (i.e., it is also an OVR-type wave). If we restrict  $\delta t_{\max}$  to 1000 days, we have 214 occultation pairs and the best-fitting pattern speed is  $1645.43^\circ \text{ d}^{-1}$ . The minimum in

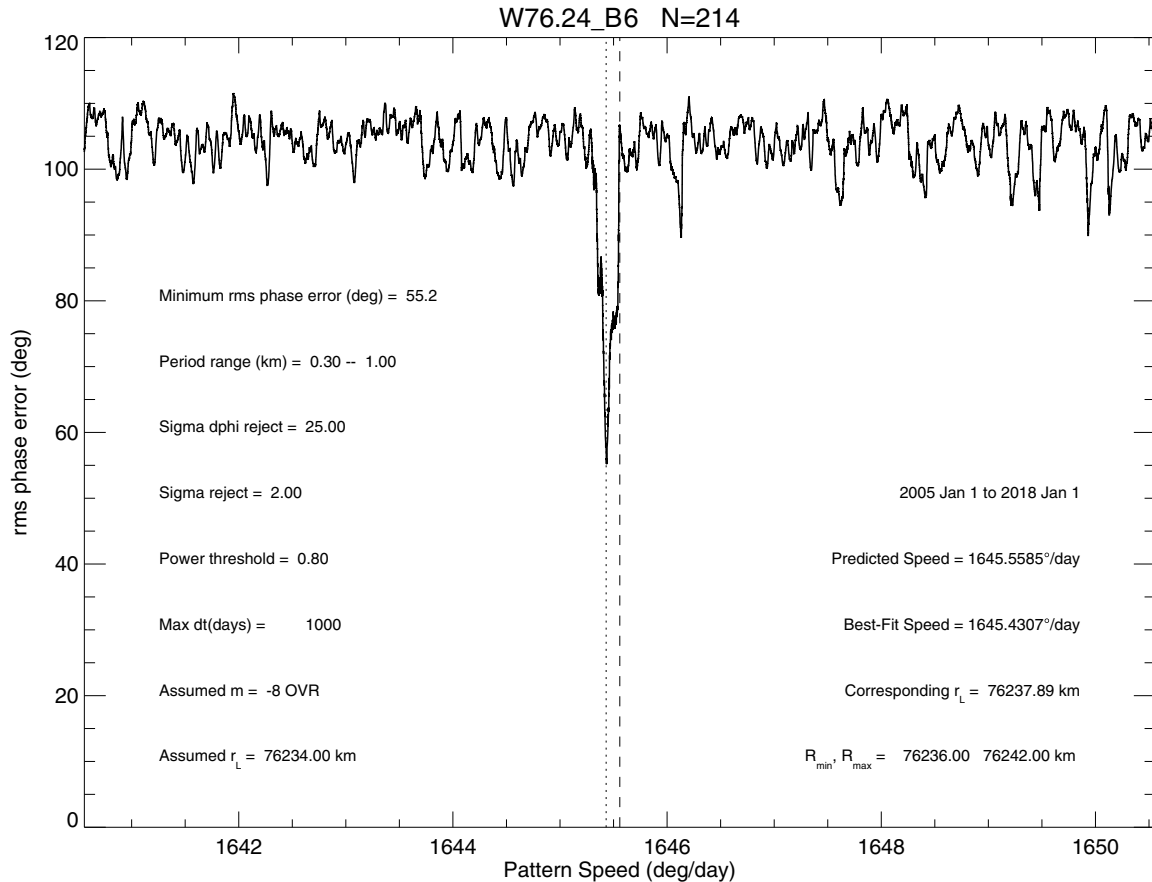


**Fig. 19.** The rms phase error  $\delta\phi_{\text{obs}} - \delta\phi_{\text{pred}}$  vs assumed wavenumber  $m = -8$  and pattern speed  $\Omega_p$ , for bending wave W76.24 (B6), using a maximum time difference of 1000 d, using 214 pairs of occultations, for an assumed resonance radius of 76234.0 km.

the rms phase residuals is 55°. The resonance radius corresponding to the pattern speed, calculated using Eq. (7), is 76237.89 km, which agrees reasonably well with Baillié et al. (2011)'s estimate of 76234 km. A plot of the rms phase residuals vs pattern speed is shown in Fig. 19.

If we now extend  $\delta t_{\text{max}}$  to 4000 days, we have 605 occultation pairs and the best-fitting pattern speed is unchanged, with a somewhat larger minimum rms phase residual of 63°. There are again several closely-spaced minima, separated by  $\sim 0.03^\circ \text{d}^{-1}$ , corresponding to one extra cycle of the 8-armed spiral pattern in a period of  $\sim 4.1$  years. The corresponding shift in the resonance radius is 0.9 km.

The identity of this wave is supported using the phase-corrected wavelet approach to characterize the wave properties, as shown in Fig. 20. The upward slope in the wavenumber vs radius plots as well as the sub-km scale wavelet profile in the bottom panel clearly show the outward propagation direction of this OVR-type wave.

## 7. Unidentified waves

In addition to the seven waves discussed above, there are several other wavelike features in the inner C ring that have so far not been identified, two of which – B10 and B11 in the catalog of Baillié et al. (2011) – are included in our list of targets and shown in Figs. 2 and 3 above. As noted in Section 3 above, the direction of propagation is uncertain for these waves. While (Baillié et al., 2011) concluded that B10 probably propagates inwards from a resonance located near 77539 km, they were unable to determine a clear direction for B11. In Fig. 21 we show a slightly larger region around each of these waves, as observed in the slow egress occultation of  $\alpha$  Canis Majoris on rev 281 where they are best-resolved. Both waves seem to be associated with narrow gaps, while both also have wavelengths that are rather short for

our data set and wavelet technique, ranging from  $\sim 0.5$  to  $1.0$  km.

The B10 wave, also designated as W76.53 in Table 2, appears to start at the gap centered at  $\sim 76531$  km and propagate inwards for  $\sim 15$  km, an unusually long distance for weak waves in the C ring. The wave is briefly interrupted by a dip in optical depth at  $\sim 76525$  km. We have so far been unable to obtain a satisfactory model for this wave, despite its prominence in many of our datasets.

The B11 wave (designated as W76.73 by Colwell et al. (2009) and in Table 2) sits atop a broader peak in optical depth centered at  $\sim 76731$  km, and is located immediately exterior to a narrow gap centered at  $\sim 76729$  km. Typically, only two or three wave cycles are visible, with no obvious trend in wavelength or amplitude to suggest the direction of propagation. We have searched for possible density or bending waves with  $2 \leq |m| \leq 20$ , but no good candidates have emerged.

Although our attempts to model these waves have so far been largely unsuccessful, it is possible that the inclusion of additional data sets or future refinements in technique may eventually permit their identification.

## 8. Surface mass densities

In principle, the identification of the wavenumber  $m$  for these waves also enables them to be used to estimate the surface mass density of various parts of the inner C ring, as we have done previously with the waves in the middle C ring (Hedman and Nicholson, 2013; 2014). However, in practice obtaining reliable surface mass densities for these extremely short-wavelength waves has been challenging. While wavelet-based methods allow the wavelengths of these waves to be estimated reliably (Tiscareno et al., 2007; Baillié et al., 2011; Hedman and

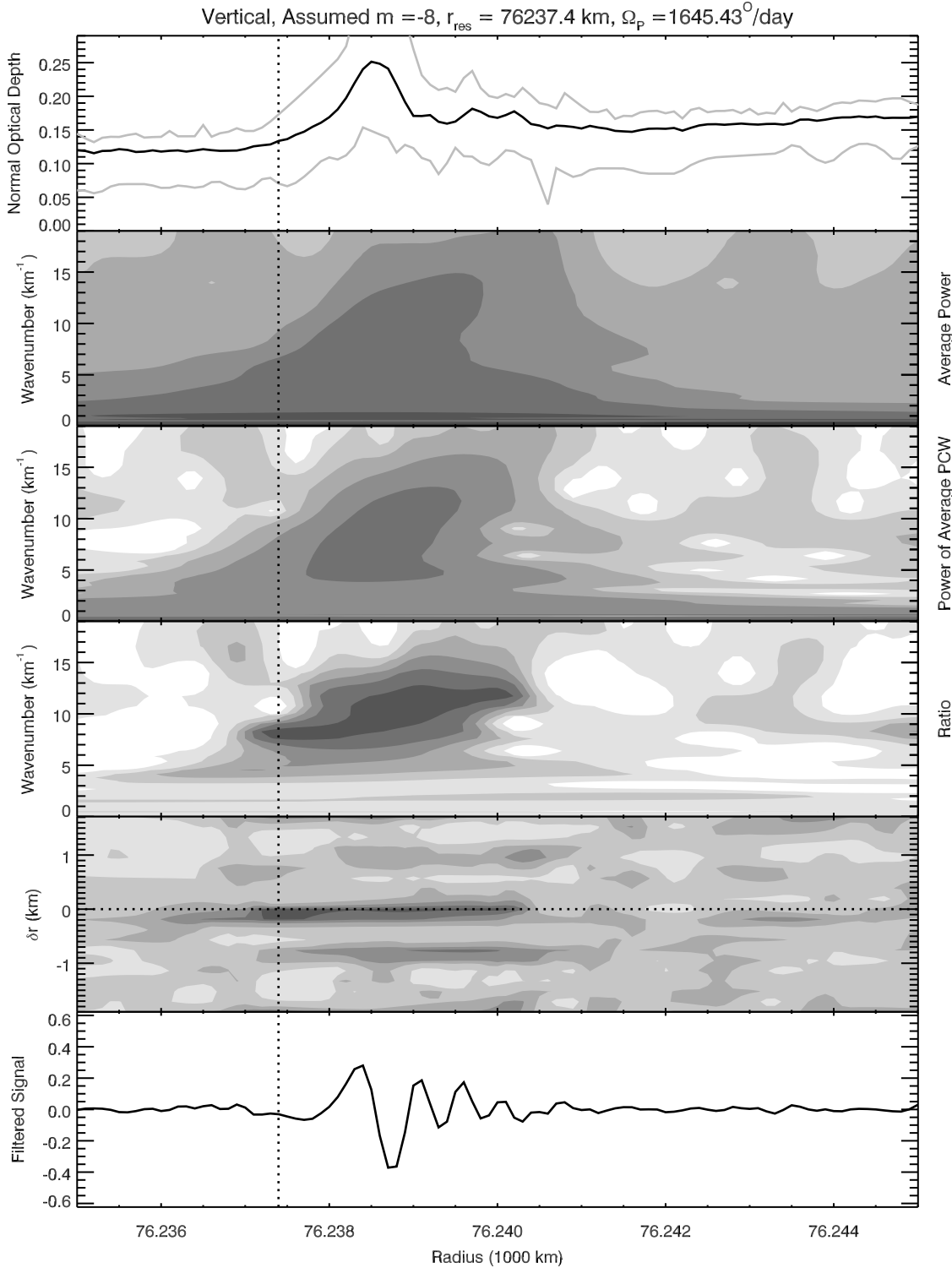


**Fig. 20.** Wavelet analysis of the OVR-type  $m = -8$  bending wave W76.24 (B6), and construction of the phase-corrected mean wave profile. See caption for Fig. 6 and text for details.

Nicholson, 2016), translating these wavelengths into surface mass density estimates requires not only knowing  $m$ , but also the distance from the exact resonance.

For a short-wavelength wave, slight uncertainties in the location of the resonance relative to the wave itself can lead to substantial systematic uncertainty in the derived mass density. For waves in regions of reasonably uniform optical depth, uncertainties in the resonance location can be ameliorated by extrapolating the observed trend of

wavelength with radius, as was done by Baillié et al. (2011), but this assumption is hazardous for most of the waves considered here, which are either near edges or on top of local peaks in surface density.

Our initial estimates of mass densities for the waves in this study yield typical values around  $0.5 – 2 \text{ g cm}^{-2}$  and opacities of order  $0.2 \text{ cm}^2 \text{ g}^{-1}$ . While these are reasonable values, we cannot provide appropriate uncertainties on these numbers until we fully quantify the systematic uncertainties in the resonance locations relative to the

**Table 3**  
Summary of wavelet analyses.

Wave (Baillié)	Resonance location <sup>a</sup> $a_{\text{res}}$ (km)	Region considered <sup>b</sup> (km)	Wavelengths considered <sup>b</sup> (km)	$dt_{\text{max}}$ (d)	$N(\delta\phi)^c$	rms( $\delta\phi$ ) min ( $\circ$ )	$m$	Type	Pattern speed $\Omega_p$ ( $^{\circ}\text{d}^{-1}$ )
W76.02	76017.94	76012–76024	0.50–1.25	1000	280	40	–9	OLR	1626.54
B5	76018.10	76012–76024	0.50–1.25	4000	839	41	–9	OLR	1626.53
W76.44	76434.29	76,425–76,437	0.50–1.25	1000	201	44	–2	OLR	2169.29
B9	76435.15 <sup>d</sup>	76,425–76,437	0.50–1.25	4000	576	46	–2	OLR	2169.26
W76.46	76459.33	76,454–76,462	0.10–1.50	1000	331	72	–7	OLR	1657.73
–	76459.58 <sup>e</sup>	76,454–76,462	0.10–1.50	300	60	28	–7	OLR	1657.72
W74.67	74666.45	74,664–74,670	0.50–1.25	1000	285	63	–7	OVR	1725.76
B1	74666.47	74,664–74,670	0.50–1.25	4000	753	67	–7	OVR	1725.76
W74.93	74935.53	74933.6–74939.6	0.30–1.00	1000	130	57	–4	OVR	1879.64
B3	74935.53	74933.6–74939.6	0.30–1.00	4000	371	61	–4	OVR	1879.64
W74.94	74941.97	74,940–74,946	0.30–1.00	1000	271	76	–9	OVR	1667.73
B4	74941.80	74,940–74,946	0.30–1.00	4000	741	71	–9	OVR	1667.74
W76.24	76237.89	76,236–76,242	0.30–1.00	1000	214	55	–8	OVR	1645.43
B6	76237.81	76,236–76,242	0.30–1.00	4000	605	63	–8	OVR	1645.43

<sup>a</sup> Determined from pattern speed, wavenumber, and wave type.

<sup>b</sup> Radial range and wavelength range considered in wavelet analysis.

<sup>c</sup> Number of  $\delta\phi$  pairs used in fit.

<sup>d</sup>  $a_{\text{res}}$  differs by + 0.86 km, compared to the  $dt_{\text{max}} = 1000$  d case.

<sup>e</sup> Using  $\gamma$  Cru occultations in 2008/9 only.

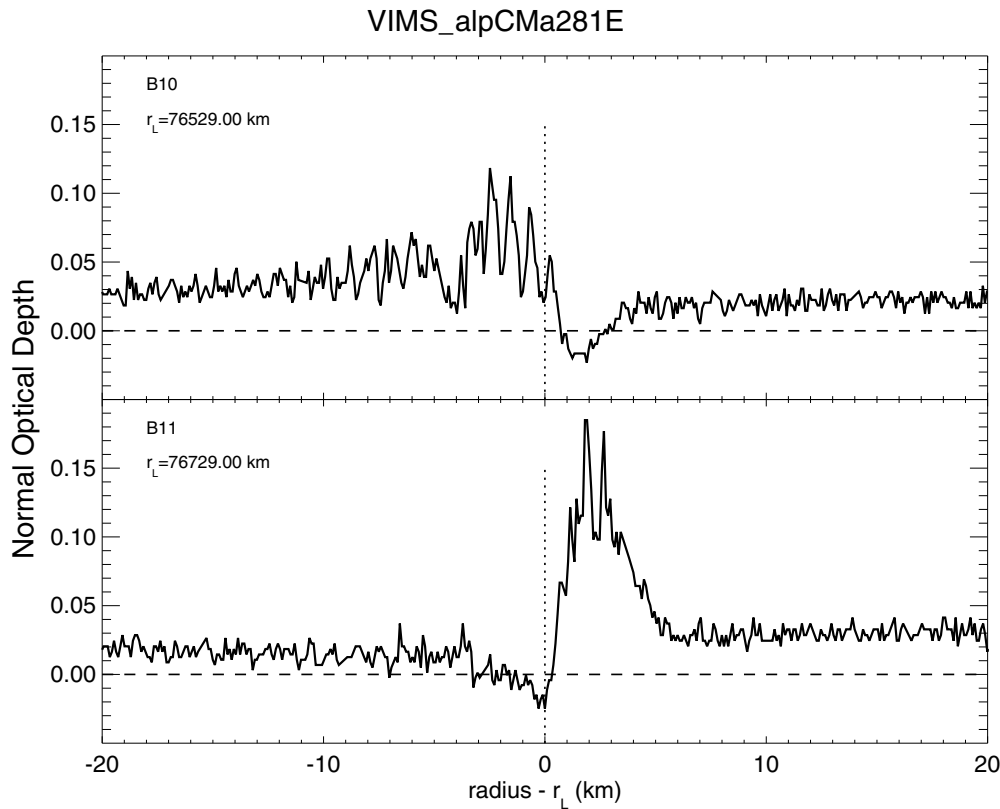


**Fig. 21.** High resolution optical depth profiles of two unidentified waves, W76.53 and W76.73 (= (Baillié et al., 2011) features B10 and B11) in the inner C ring, as observed in the egress occultation of  $\alpha$  Canis Majoris on rev 281, on 27 June 2017. Nominal resonance radii are from Table 2, but the directions of propagation remain uncertain. The absolute radius scale is also uncertain by several km, due to difficulties in navigating occultations by this visual binary star.

waves. This will likely require a more careful evaluation of both the absolute ring geometry and subtle shifts in the apparent resonance locations due to phenomena such as the strong Titan apsidal resonance, and is beyond the scope of the present work.

## 9. Discussion and conclusions

Our investigation of the tightly-wrapped waves in the inner C ring has resulted in the identification of three additional density waves (W76.02 = B5, W76.44 = B9 and W76.46) apparently driven by normal mode oscillations in Saturn, to add to the nine already identified

by Hedman and Nicholson (2013, 2014) and French et al. (2016). More significantly, we have also identified the first bending waves driven by such internal oscillations: W74.67 = B1, W74.93 = B3, W74.94 = B4 and W76.24 = B6. All of these identifications are based on the three observational parameters that can be derived from the wave profiles: their  $m$ -values (or number of spiral arms), their pattern speeds  $\Omega_p$ , and their directions of propagation. The  $m$ -values for the newly-identified waves range from 2 to 9.

Following Marley and Porco (1993), we make the reasonable assumption that an  $m$ -armed spiral wave can only be driven by a normal mode that exhibits  $m$ -fold symmetry in longitude. Planetary internal

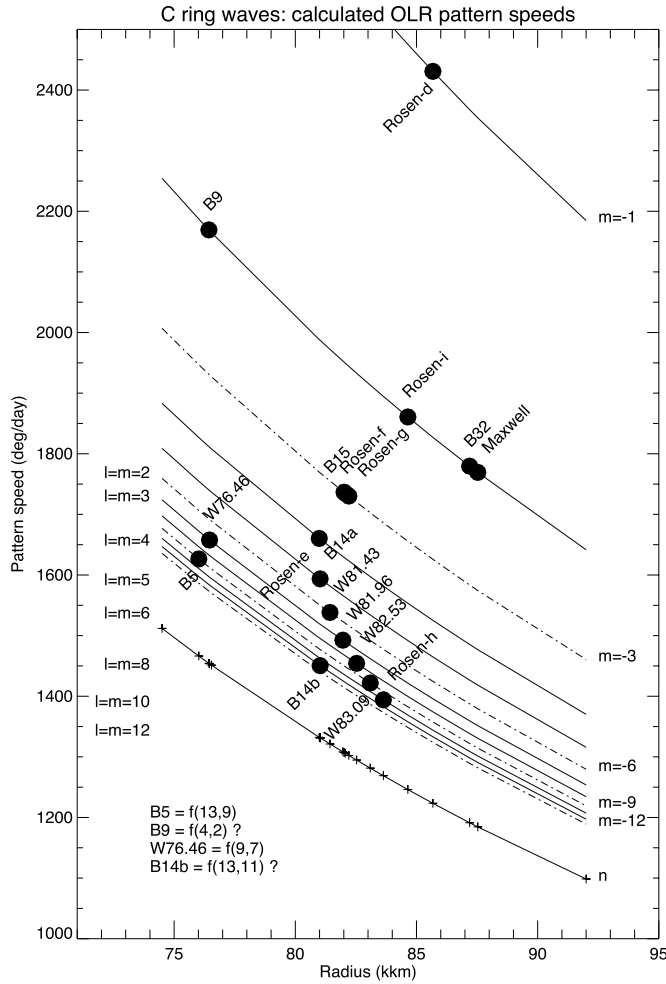


**Fig. 22.** An updated summary of density waves in the C ring identified with OLRs driven by internal normal mode oscillations in Saturn (*f*-modes). The abscissa is orbital radius in units of 1000 km and the ordinate is the pattern speed of the modes. Filled circles indicate waves with known  $m$ -values, labelled by their numbers in the catalogues of Rosen et al. (1991) or Baillié et al. (2011), while diagonal curves show the predicted pattern speed,  $\Omega_p$  as a function of radius for  $-12 \leq m \leq -1$ , as well as the keplerian mean motion,  $n$ . Our new results for the B5 (W76.02), B9 (W76.44) and W76.46 waves are from Table 3.

modes, however, are classified by their values of both  $\ell$  and  $m$ , as described in Section 2 above, and their periods and pattern speeds depend on both parameters. Although we expect density waves to be driven by normal modes with even values of  $\ell - m$ , and bending waves by modes with odd values of  $\ell - m$ , we cannot directly derive the values of  $\ell$  from the wave observations. Instead, we must rely on comparisons of the observed values of  $\Omega_p$  with those predicted from theoretical calculations of mode frequencies.

A notable feature of the fits shown above is that, while the density and bending waves have generally similar amplitudes in the occultation profiles, the minimum rms residuals are quite a bit smaller for the former. We attribute this to our oversimplified treatment of the bending waves, in which we simply add  $180^\circ$  to the predicted phase whenever the parameter  $\beta$  is negative. A more realistic model, which we have not yet implemented, would use the actual values of  $B_*$  and  $\phi$  for each observation to predict the appearance of the wave and thus its apparent optical depth profile and finally its phase as measured by the wavelet transform. Such a model would also be valuable in permitting quantitative estimates of wave amplitudes, which we have not so far attempted for density or bending waves.

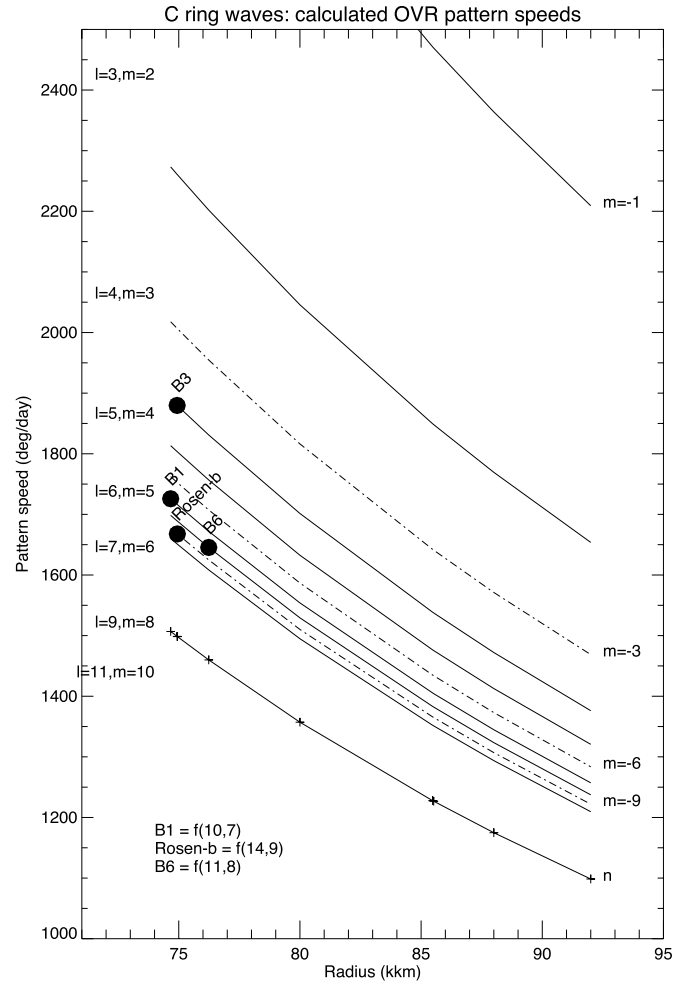


**Fig. 23.** A summary of bending waves in the C ring identified with OVRs driven by internal normal mode oscillations in Saturn (*f*-modes). The abscissa is orbital radius in units of 1000 km and the ordinate is the pattern speed of the modes. Filled circles indicate waves with known  $m$ -values, labelled by their numbers in the catalogues of Rosen et al. (1991) or Baillié et al. (2011), while diagonal curves show the predicted pattern speed,  $\Omega_p$  as a function of radius for  $-10 \leq m \leq -2$ , as well as the keplerian mean motion,  $n$ . Our new results for the B1 (W74.67), B3 (74.93), B4 (W74.94, or Rosen-b) and B6 (W76.24) waves are from Table 3.

**Fig. 22** puts our new results on density waves driven by saturnian normal modes in the context of previous identifications. We plot here the observed values of pattern speed and resonance radius for each wave, superimposed on a set of curves which show how  $\Omega_p$  varies with  $r$  for  $-12 \leq m \leq -1$ , from Eq. (5). Also shown are the predicted pattern speeds for saturnian *f*-modes with  $\ell = m$  and  $2 \leq m \leq 12$ , as calculated by C. Mankovich (priv. comm, 2017).<sup>5</sup>

The actual picture is complicated by the fact that three different density waves have previously been identified with  $m = -2$  (Hedman and Nicholson, 2013; French et al., 2016), and another three waves with  $m = -3$  (Hedman and Nicholson, 2013). The reason for this multiplicity of waves when only a single forcing frequency is expected is unknown, although it has been suggested that it may involve non-linear mixing of *f* and *g*-modes in a non-convective layer outside

<sup>5</sup> Recall that we use negative values of  $m$  to describe OLR- or OVR-type resonances and waves, but that these are expected to be driven by prograde normal modes with  $m_* = |m|$ . Here we use the conventional positive values of  $m$  in describing the normal modes, to avoid any potential confusion with retrograde modes for which  $m_*$  is negative.

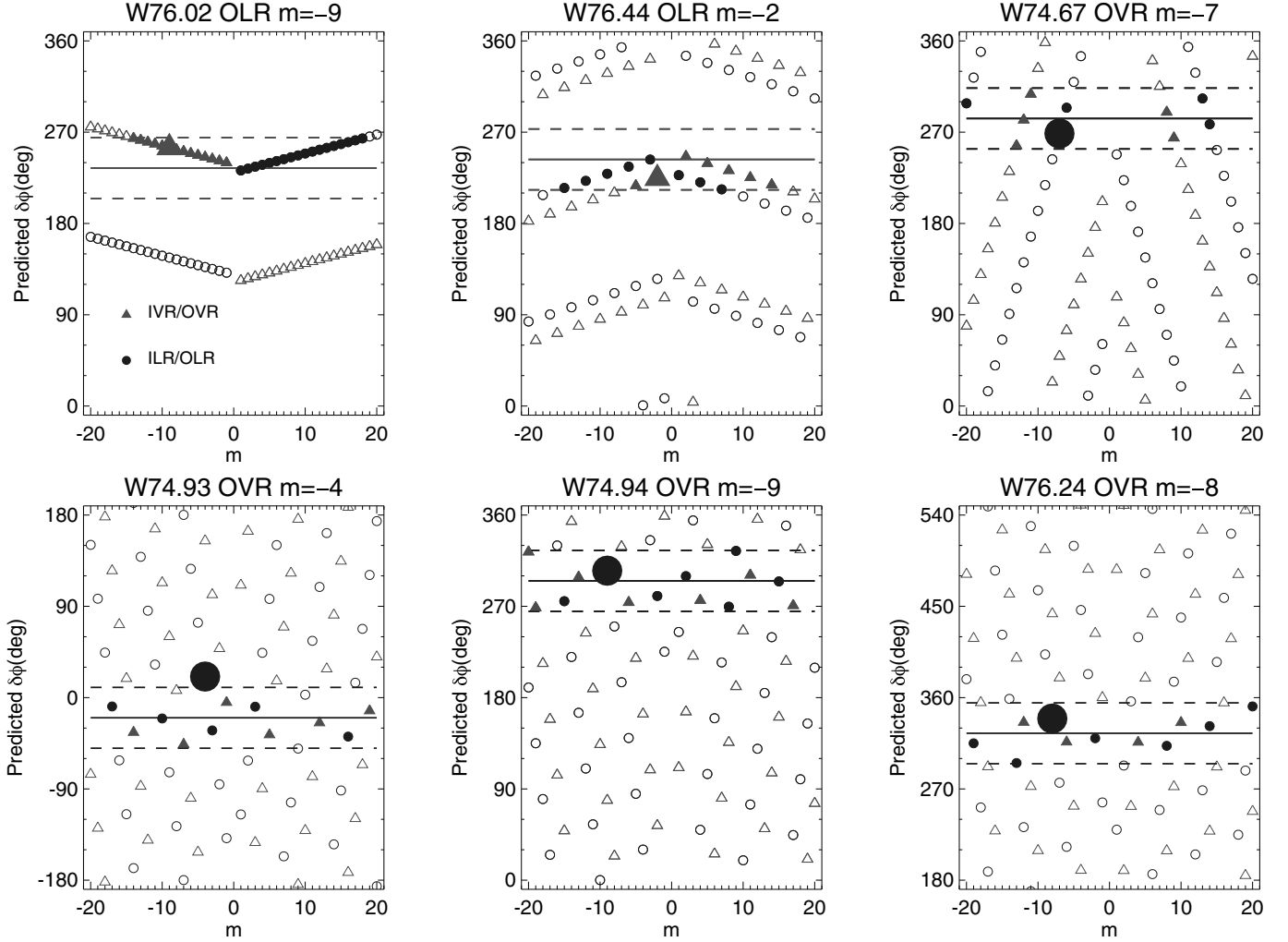


**Fig. 24.** Graphical tests of the assignment of  $m$ -values to six of the waves identified in our study, using the pair of  $\gamma$  Crucis occultations on revs 100 and 101. The predicted phase differences between the wave profiles are shown for wavenumber between  $m = -20$  and  $+20$ , for both vertical resonances IVR/OVR (red) and density waves (ILR/OLR, shown in blue). In each panel, the horizontal line marks the measured phase difference between the profiles for the labeled wave. Wavenumbers for which the predicted and observed phase differences lie within a cutoff range of  $\pm 30^\circ$  (bounded by the pair of dashed lines) are shown as filled symbols, and are regarded as candidate wavenumbers and wave types for this wave, based solely on the criterion of matching phase. The large filled symbol marks the predicted phase and wavenumber for the putative wave in each panel, as identified in Table 3. See text for additional details. (For interpretation of the references to color in this figure legend, the reader is referred to the web version of this article.)

Saturn's rocky core (Fuller et al., 2014). At any rate, all three  $m = -3$  waves have pattern speeds that are very similar and quite close to the expected rate. For  $m = -2$  the situation is less clear, but two of the three reported waves do have frequencies fairly close to the expected rate. The single  $m = -4$  and  $m = -10$  waves reported by Hedman and Nicholson (2013) and Hedman and Nicholson (2014) also seem to match the predicted values of  $\Omega_p$  for  $\ell = m = 4$  and  $\ell = m = 10$ .

When we look at the pattern speeds of the three newly-identified density waves, and their resonance locations in Fig. 22, it is immediately evident that their pattern speeds are far too high to be consistent with sectoral (i.e.,  $m = \ell$ ) modes, and no fundamental sectoral ( $\ell = m$ ) normal modes are expected to produce resonances in the inner part of the C ring. However, Saturn's fundamental normal mode spectrum is also expected to contain many non-sectoral modes that are predicted to generate resonances in this region (Marley and Porco, 1993; Mankovich et al., 2017). In fact, the locations of all but one of the waves identified here are very close to the predicted locations of resonances with non-sectoral normal modes. While we cannot independently determine the  $\ell$  values for any of planetary modes with just the ring data, the overall consistency between our observations and theoretical predictions makes the mode identifications relatively

secure.

In particular, it is likely that these waves represent higher-frequency non-sectoral modes with  $m = \ell - 2$  or  $m = \ell - 4$ . Preliminary calculations (Mankovich et al., 2017) indicate that the W76.02 (B5) wave may in fact be identified with the  $(\ell = 13, m = 9)$  normal mode and the W76.44 wave with the  $(\ell = 9, m = 7)$  mode. The pattern speed of the W76.44 (B9) wave is unusually high at  $2169.3^\circ \text{ d}^{-1}$ , and this wave remains unidentified (a preliminary identification with the  $\ell = 4, m = 2$  mode was in error). These tentative identifications are indicated in Fig. 22. Based on Fig. 22 and C. Mankovich's predicted frequencies (2017 priv. comm.), it may also be possible to have ILR-type density waves driven by saturnian  $f$ -modes in the inner C ring, at least for  $m \geq 11$ .

Fig. 23 presents the equivalent diagram for bending waves, where the observed wave parameters are now compared with those predicted for  $f$ -modes with  $m = \ell - 1$ . No previous identifications of bending waves driven by saturnian normal modes have been reported, so the only waves shown in Fig. 23 are those reported in Table 3. Of the four bending waves we have analyzed, only the W74.93 (B3) wave has a pattern speed and resonance radius consistent with that expected for  $m = \ell - 1$  modes. Specifically, the  $\ell = 5, m = 4$  mode is predicted to

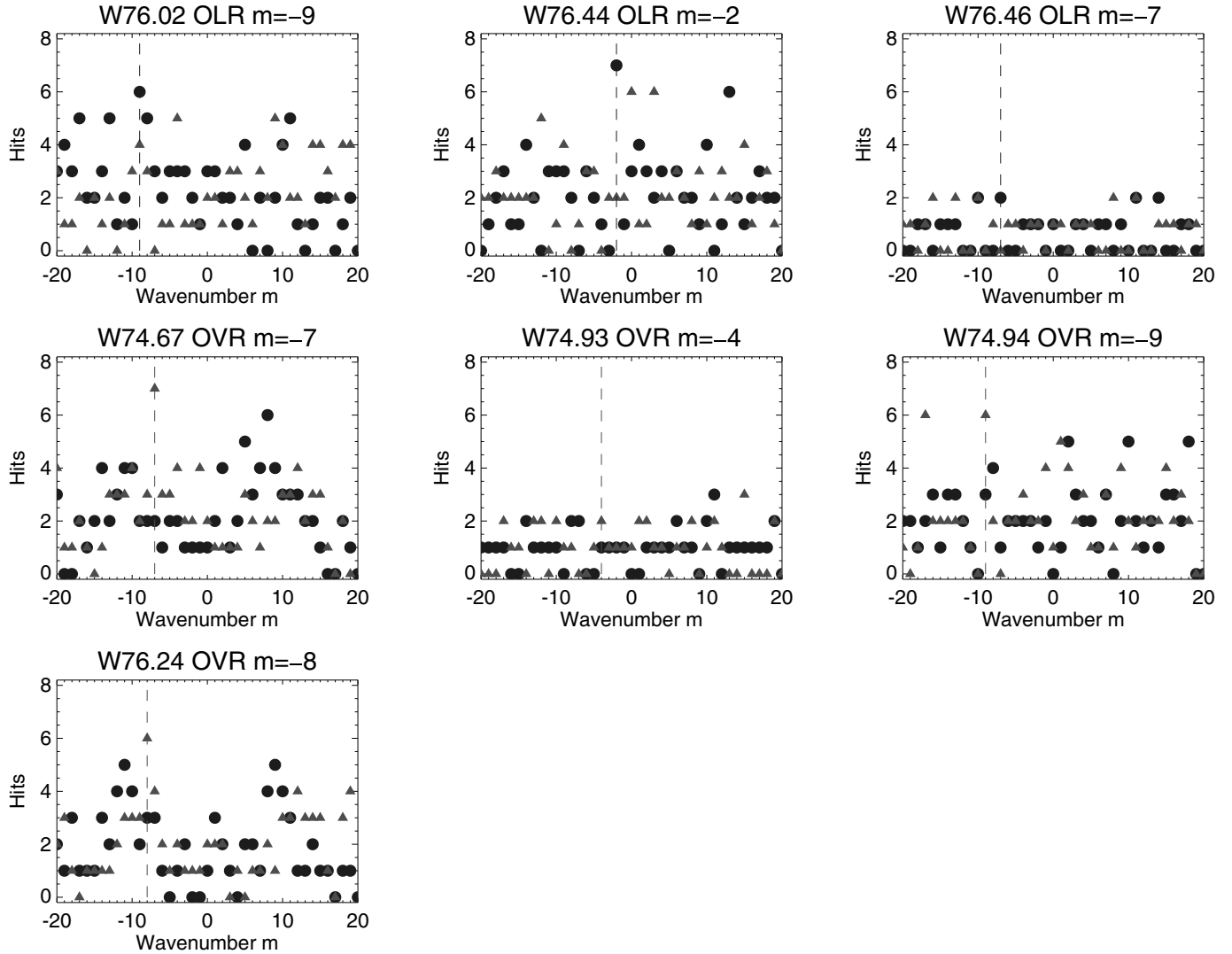


**Fig. 25.** Accumulated number of instances (hits) of measured phase differences between seven pairs of occultation profiles lying with  $\pm 60^\circ$  of the predicted value for wavenumbers  $m = -20$  to  $+20$ , for the seven waves of this study. Vertical (IVR/OVR) resonances are shown in red, and density waves (ILR/OLR) are shown in blue. The dashed vertical lines mark the proposed wavenumber and color-coded wave type for each wave. See text for additional details. (For interpretation of the references to color in this figure legend, the reader is referred to the web version of this article.)

have a pattern speed of  $\sim 1869^\circ \text{ d}^{-1}$ , very close to that of the W74.93 (B3) wave that is observed to have  $m = -4$  and  $\Omega_p = 1879.6^\circ \text{ d}^{-1}$ .

It is possible that the other three bending waves represent higher-frequency modes with  $m = \ell - 3$  or  $m = \ell - 5$ . Preliminary calculations suggest that the observed pattern speeds can be matched by the  $(\ell = 10, m = 7)$  mode for B1, by the  $(\ell = 11, m = 8)$  mode for B6 and by the  $(\ell = 14, m = 9)$  mode for B4 (= Rosen b) (Mankovich et al., 2017). Again, it may also be possible to have IVR-type bending waves driven by saturnian  $f$ -modes in the inner C ring, at least for larger values of  $m$ .

Hedman and Nicholson (2014) pointed out that while the planetary normal modes with  $\ell = m = 2, 3, 4$  and  $10$  all generate clear waves in the rings, density waves generated by sectoral modes with  $5 \leq m \leq 9$  are not obvious, indicating that the latter modes must have much lower amplitudes. By itself, our discovery of an  $m = 9$  wave that may correspond to the  $(\ell = 13, m = 9)$  normal mode expands the range of missing waves to include those associated with other potential non-sectoral modes. It appears that the situation *vis a vis* bending waves is similar, with only a single wave with  $m = \ell - 1$  being identified but three others with  $m = \ell - 3$  or  $\ell - 5$ . However, a recent study (Hedman et al., 2018) using refined wavelet algorithms has indeed

uncovered several additional weaker waves, helping to fill in the gaps in the observed suite of modes.

In this context, we end by noting that several additional waves have been noted in the VIMS data (such as the B10 and B11 waves illustrated in Fig. 21 above), but remain as yet unidentified. Phase-correcting techniques such as those described by Hedman and Nicholson (2016) could reveal even weaker waves. Looking beyond the VIMS observations, additional wave characterizations might well be possible using UVIS ring occultation data, which have higher radial resolution than the VIMS data, with appropriate processing to co-add data coherently from multiple occultations. The optical depth profiles derived from ring occultations observed using the Radio Science Subsystem (RSS) experiment on Cassini also hold promise, once they have undergone the extensive processing required to achieve accurate sub-km resolution.

#### Acknowledgments

We are grateful to two anonymous reviewers for their helpful clarifying comments. This work was supported in part by NASA through the Cassini Data Analysis Program NNX17AF85G, and through Cassini project support to the RSS and VIMS science teams. We are grateful for

helpful conversations with Ethan Dederick, Mark Marley, and Chris Mankovich concerning the possible associations of our newly-detected waves and specific internal oscillations of Saturn. We would also like to

acknowledge the work done by the VIMS engineering and science teams to build and operate the instrument, and to collect the occultation data used herein.

## Appendix A. Confirmation of wave identifications

In carrying out the fits described in Sections 5 and 6 above, one must be alert to the possibility of alternate solutions involving spiral waves with different  $m$ -values. Our usual procedure is to explore all values of  $m$  between  $-20$  and  $20$  for each wave, with a range of  $\Omega_p$  spanning  $\pm 20^\circ$  relative to that predicted by Eq. (5) or Eq. (7), depending on whether a density or bending wave is involved. In almost all cases, a deep minimum in the rms residuals is found for only a single value of  $m$  anywhere in the vicinity of the predicted rate. In instances where the nature of the wave is uncertain, such as feature B11 in Fig. 21, we run models for both density and bending waves.

Nevertheless, it seems prudent to determine, after the fact, whether the value of  $m$  identified for a particular wave is the only (or best) plausible solution. One way to do this is to exploit the fact that we have several pairs of occultations with similar geometry and closely spaced in time that can be used to test the nominal best-fit model for each wave, and check for previously overlooked alternatives. Using occultations with small values of  $\delta t$  ensures that our phase matches are relatively insensitive to the exact pattern speed assumed, and if we compare only events involving the same star with similar geometry then variations in data quality and resolution are minimized.

Two types of observation satisfy the above criteria: individual chord occultations that involve both ingress and egress cuts of the same radial ranges, and similar occultations by the same star on adjacent Cassini orbits. If we further restrict our attention to bright stars that yield profiles with high signal-to-noise ratios, we find a total of seven useful pairs of events distributed across the duration of the mission, from rev 100 to rev 245. For each pair of occultations, and each wave, we compare graphically the measured and predicted phase differences,  $\delta\phi$  for a range of plausible  $m$ -values. Such a plot is shown in Fig. 24 for six of the waves, using the  $\gamma$  Crucis occultations on revs 100 and 101 (feature W76.46 is omitted because of a data gap in the observations that prevents a reliable wavelet decomposition of the wave). For each suspected wave and wave type (density wave or bending wave), we compute the predicted phase difference for wavenumber  $m$  from  $-20$  to  $+20$ . In this figure, each panel shows the predicted values of  $\delta\phi$  (red triangles for vertical resonances IVR/OVR; blue circles for density waves ILR/OLR) as a function of the assumed value of  $m$ , based on the predicted pattern speeds and the known values of  $\delta t$  and  $\delta\lambda$ , via Eq. (12). The predicted phase difference for our preferred value of  $m$  is indicated by the large filled symbol. Superimposed on this array of predictions is the measured phase difference provided by our wavelet analysis, indicated by the horizontal solid line, color-coded to match the proposed wave type. Filled symbols correspond to wavenumbers of either type of wave for which the predicted phase difference lies within a cutoff range of  $\pm 30^\circ$  of the measured value, and we regard these as candidate wavenumbers and wave types for the observed wave in each case. (The unfilled symbols lie outside of this cutoff range.)

Checking Fig. 24, we find that the observed phase difference for W76.02 (B5) is consistent with a broad range of possible OVR wavenumbers ( $m = 1 - 14$ ), including our proposed wavenumber  $m = -9$ , but also consistent with ILR wavenumbers  $m = 1 - 18$ . This particular pair of observations is not a useful discriminator of possible wavenumbers for this wave. On the other hand, for W76.44 (B9), only a few wavenumbers lie within the cutoff range, including our preferred OLR  $m = -2$  value. This is the case, too, for the remaining four waves shown, although for W74.93 (B3), the observed phase difference for this particular pair of occultation profiles differs by more than  $30^\circ$  from the predicted value.

Proceeding in a similar fashion for all seven pairs of events and all seven waves in this study, we tabulated for each wavenumber and wave type the total number of instances (or hits) in which the measured phase difference was within ( $\pm 60^\circ$ ) of the predicted value, as summarized in Fig. 25. For each wave, the vertical dashed line marks the preferred wavenumber, color coded by wave type (blue for OLR, red for OVR), and the individual symbols mark the number of instances (out of a maximum possible of seven) in which the measured phase was within the cutoff range. For W76.44 and W74.67, the measured phase differences matched the predictions for our proposed wavenumber and wave type ( $m = -2$ , OLR for W76.44;  $m = -7$ , OVR for W74.67), within the specified range of uncertainty, for all seven occultation pairs. For these two waves, no other combination of wavenumber or wave type matched this success rate. For W76.02 and W76.24, the proposed wavenumber and wave type yielded six hits, unmatched by any other combination of waves and wave types. These first four wave identifications therefore seem to be independently confirmed and relatively secure. For W76.46 and W74.94, the proposed wavenumbers and wave types each share a maximum number of hits with other combinations of wavenumbers and wave types, but for none of these first six waves did we find an alternative value of  $m$  which is preferred over the value listed in Table 3. Only for W74.93 was the number of hits so small for any combination of wavenumbers and wave types that the results were uncertain.

Overall, we consider this test to be a success, with most of the wave identifications being relatively secure, if not certain, based solely on a comparison of seven independent pairs of occultation profiles. In the end, of course, our pattern speed scanning method utilized many more independent pairs (60 to 839, as shown in Table 3), and the strongest evidence in favor of any given ring identification is the observed sharp minimum in the rms phase error near the expected pattern speed for a given wavenumber and resonance type.

## References

- Acton, C., Bachman, N., Semenov, B., Wright, E., 2018. A look towards the future in the handling of space science mission geometry. *Planet. Space Sci.* 150, 9–12.
- Acton, C.H., 1996. Ancillary data services of NASA's navigation and ancillary information facility. *Planet. Space Sci.* 44, 65–70.
- Baillié, K., Colwell, J.E., Lissauer, J.J., Esposito, L.W., Sremčević, M., 2011. Waves in Cassini UVIS stellar occultations. 2. The C ring. *Icarus* 216, 292–308.
- Brown, R.H., 2004. The Cassini visual and infrared mapping spectrometer (VIMS) investigation. *Space Sci. Rev.* 115, 111–168. 21 colleagues.
- Colwell, J.E., Nicholson, P.D., Tiscareno, M.S., Murray, C.D., French, R.G., Marouf, E.A., 2009. The structure of Saturn's rings. In: Dougherty, M., Krimigis, S. (Eds.), *Saturn after Cassini-Huygens*. Springer, pp. 375–412.
- Esposito, L.W., Cuzzi, J.N., Holberg, J.B., Marouf, E.A., Tyler, G.L., Porco, C.C., 1984. *Saturn's rings - structure, dynamics, and particle properties*. In: *Saturn (A85-33976 15-91)*. Tucson, AZ, University of Arizona Press, pp. 463–545.
- French, R.G., Marouf, E.A., Rappaport, N.J., McGhee, C.A., 2010. Occultation observations of Saturn's B ring and Cassini division. *Astron. J.* 139, 1649–1667.
- French, R.G., McGhee-French, C.A., Lonergan, K., Sepersky, T., Jacobson, R.A., Nicholson, P.D., Hedman, M.M., Marouf, E.A., Colwell, J.E., 2017. Noncircular features in Saturn's rings IV: absolute radius scale and Saturn's pole direction. *Icarus* 290, 14–45.
- French, R.G., Nicholson, P.D., Hedman, M.M., Hahn, J.M., McGhee-French, C.A., Colwell, J.E., Marouf, E.A., Rappaport, N.J., 2016. Deciphering the embedded wave in Saturn's maxwell ringlet. *Icarus* 279, 62–77.
- Fuller, J., Lai, D., Storch, N.J., 2014. Non-radial oscillations in rotating giant planets with solid cores: application to Saturn and its rings. *Icarus* 231, 34–50.
- Gresh, D.I., Rosen, P.A., Tyler, G.L., Lissauer, J.J., 1986. An analysis of bending waves in Saturn's rings using voyager radio occultation data. *Icarus* 68, 481–502.
- Hedman, M.M., Nicholson, P.D., 2013. Kronoseismology: using density waves in Saturn's c ring to probe the planet's interior. *Astron. J.* 146, 12.
- Hedman, M.M., Nicholson, P.D., 2014. More kronoseismology with Saturn's rings. *Mon. Not. R. Astron. Soc.* 444, 1369–1388.
- Hedman, M.M., Nicholson, P.D., 2016. The B-ring's surface mass density from hidden density waves: less than meets the eye? *Icarus* 279, 109–124.
- Hedman, M.M., Nicholson, P.D., French, R.G., 2018. Kronoseismology IV: six previously unidentified waves in Saturn's middle C ring. *Astron. J.* in press.
- Mankovich, C., Marley, M. S., Fortney, J. J., Movshovitz, N., 2018. Saturn's internal

- structure: a view through its natural seismograph. In: Proceedings of the AAS/Division for Planetary Sciences Meeting Abstracts #49 49, 303.06.
- Marley, M.S., 2014. Saturn ring seismology: looking beyond first order resonances. *Icarus* 234, 194–199.
- Marley, M.S., Porco, C.C., 1993. Planetary acoustic mode seismology – Saturn's rings. *Icarus* 106, 508.
- Nicholson, P.D., Cooke, M.L., Pelton, E., 1990. An absolute radius scale for Saturn's rings. *Astron. J.* 100, 1339–1362.
- Nicholson, P.D., French, R.G., McGhee-French, C.A., Hedman, M.M., Marouf, E.A., Colwell, J.E., Lonergan, K., Sepersky, T., 2014. Noncircular features in Saturn's rings: II. The C ring. *Icarus* 241, 373–396.
- Nicholson, P.D., Hedman, M.M., 2016. A vertical rift in Saturn's inner C ring. *Icarus* 279, 78–99.
- Nicholson, P.D., Porco, C.C., 1988. A new constraint on Saturn's zonal gravity harmonics from voyager observations of an eccentric ringlet. *J. Geophys. Res.* 93, 10209–10224.
- Porco, C., Nicholson, P.D., Borderies, N., Danielson, G.E., Goldreich, P., Holberg, J.B., Lane, A.L., 1984. The eccentric saturnian ringlets at 1.29 r(s) and 1.45 r(s). *Icarus* 60, 1–16.
- Rosen, P.A., Lissauer, J.J., 1988. The titan – 1:0 nodal bending wave in Saturn's ring C. *Science* 241, 690–694.
- Rosen, P.A., Tyler, G.L., Marouf, E.A., Lissauer, J.J., 1991. Resonance structures in Saturn's rings probed by radio occultation. II - results and interpretation. *Icarus* 93, 25–44.
- Shu, F.H., 1984. Waves in planetary rings. In: Brahic, A., Greenberg, R. (Eds.), In IAU Colloq. 75: Planetary Rings. Univ. of Arizona Press, pp. 513–561.
- Shu, F.H., Cuzzi, J.N., Lissauer, J.J., 1983. Bending waves in Saturn's rings. *Icarus* 53, 185–206.
- Tiscareno, M.S., Burns, J.A., Nicholson, P.D., Hedman, M.M., Porco, C.C., 2007. Cassini imaging of Saturn's rings. II. a wavelet technique for analysis of density waves and other radial structure in the rings. *Icarus* 189, 14–34.